

Yu-Shiba-Rusinov qubit

Archana Mishra,^{1,*} Pascal Simon,^{2,†} Timo Hyart,^{1,3,‡} and Mircea Trif^{1,§}

¹*International Research Centre MagTop, Institute of Physics,*

Polish Academy of Sciences, Aleja Lotników 32/46, PL-02668 Warsaw, Poland

²*Université Paris-Saclay, CNRS, Laboratoire de Physiques des Solides, 91405, Orsay, France*

³*Department of Applied Physics, Aalto University, 00076 Aalto, Espoo, Finland*

(Dated: December 14, 2021)

Magnetic impurities in s -wave superconductors lead to spin-polarized Yu-Shiba-Rusinov (YSR) in-gap states. Chains of magnetic impurities offer one of the most viable routes for the realization of Majorana bound states which hold a promise for topological quantum computing. However, this ambitious goal looks distant since no quantum coherent degrees of freedom have yet been identified in these systems. To fill this gap we propose an effective two-level system, a YSR qubit, stemming from two nearby impurities. Using a time-dependent wave-function approach, we derive an effective Hamiltonian describing the YSR qubit evolution as a function of distance between the impurity spins, their relative orientations, and their dynamics. We show that the YSR qubit can be controlled and read out using state-of-the-art experimental techniques for manipulation of the spins. Finally, we address the effect of spin noise on the coherence properties of the YSR qubit, and show a robust behaviour for a wide range of experimentally relevant parameters. Looking forward, the YSR qubit could facilitate the implementation of a universal set of quantum gates in hybrid systems where they are coupled to topological Majorana qubits.

I. INTRODUCTION

The goal to build a fault tolerant quantum computer has allowed to deepen the understanding of the quantum realm in a plethora of systems, as well as to an advancement in developing novel quantum technologies. Trapped ions, semiconductor quantum dots, superconducting circuits and hybrid semiconductor-superconductor platforms are some of the examples which have played crucial role in developing the field of quantum computing [1–14].

While superconducting-circuit based qubits have been at the forefront of the immense recent progress, proposals that utilize the low-energy bound states in superconductors, i. e. the Andreev levels, have been also under intense scrutiny for quantum computing [15–21]. The reasons are two-fold: (i) the dimensions of Andreev states-based qubits ($\sim \mu\text{m}$) are typically much smaller than the sizes of the conventional superconducting qubits ($\sim \text{mm}$), which facilitates designing quantum registers with higher qubit densities and (ii) they constitute the building blocks of topological quantum computers based on Majorana zero modes, which have experienced significant theoretical and experimental research efforts [22–27].

Magnetic impurities in superconductors lead to localised Yu-Shiba-Rusinov (YSR) in-gap Andreev states [28–34], with chains and lattices of impurities being viable setups to realize topological superconductors hosting the Majorana modes [35–58]. The advantage of these implementations is rooted in the ability to pattern super-

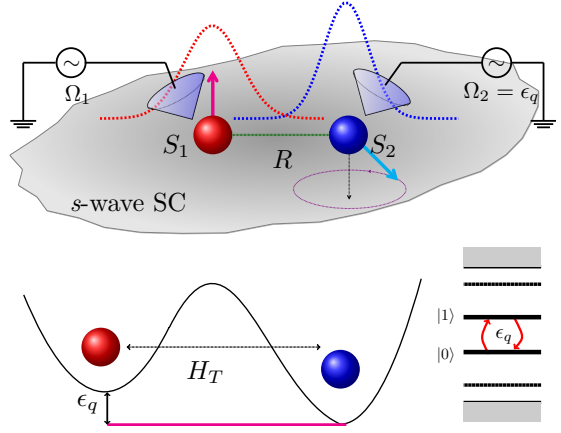


FIG. 1. The YSR qubit: Two classical spins, target (red) and test (blue), are placed on top of a 2D s -wave superconductor at a distance R inducing a double-well potential that accommodates two in-gap YSR states for a given parity. The odd parity states $|0\rangle$ and $|1\rangle$ define the YSR qubit states. The asymmetry of the potential stems from the slightly different coupling parameters at the two sites. The hybridization of the two YSR states is quantified by a tunneling Hamiltonian H_T . Driving the test spin effectively tunes the potential bias and, when at resonance with the qubit splitting $\Omega_2 = \epsilon_q$, it allows for coherent rotations of the qubit. The target spin is interrogated off-resonantly at a frequency $\Omega_1 \neq \epsilon_q$ for quantum non-demolition detection of the YSR qubit state. Alternatively, the qubit can be also operated with just a single tip.

conducting surfaces with magnetic impurities, and possibly engineer (topological) quantum processors in a controlled fashion. Moreover, through the use of scanning tunneling microscopy (STM) techniques, they can be interrogated locally, with high spatial resolution. A drawback, however, is that the system parameters are hard to

* mishra@MagTop.ifpan.edu.pl

† pascal.simon@u-psud.fr

‡ Timo.Hyart@MagTop.ifpan.edu.pl

§ mtrif@MagTop.ifpan.edu.pl

tune making it difficult to control the topological regime of the system, or to manipulate the emerging Majorana modes. Several solutions have been put forward, among which are exploiting the dynamics of the magnetic impurities [59, 60], driving the YSR states with microwave fields [61], varying the orientation of external magnetic fields [62, 63], or tuning the Josephson effect through a superconducting tip coupled to the YSR states [64].

The realization of the Majorana-based topological quantum computer in Shiba chains looks distant as no experimental evidence of quantum degrees of freedom yet exist in these systems. For this purpose it would be necessary to experimentally demonstrate that it is possible to coherently manipulate the Majorana qubits before they decohere. In this paper, we show that the minimal system for the demonstration of the quantumness of these systems is a new type of superconducting qubit, the YSR qubit, stemming from two nearby impurities. We demonstrate that the dynamics of the magnetic impurities can be used for controlling the quantum state of the YSR qubit and we uncover the requirements for experimentally observing Rabi oscillations in this system. The precession of the magnetic impurities also leads to a feedback torque acting on the impurities due to the YSR states [65], and we show that this effect can be utilized for the read out of the YSR qubit states. We also address the effect of the spin noises on the coherence properties of the YSR qubit, and show a robust behaviour for a wide range of experimentally relevant parameters. Our proposal is feasible with state-of-the-art experimental techniques, because controlled coupling of YSR states in impurity dimers have already been experimentally demonstrated [66–69] and the manipulation of the impurity spins is possible through the STM electron spin resonance (STM-ESR) techniques [70–74]. Finally, we discuss the possibilities to utilize the YSR qubits in hybrid systems where they are coupled to Majorana qubits.

The paper is organized as follows. In Sec. II we introduce the model Hamiltonian describing the dynamical spin dimer. Using a time-dependent wave-function approach, in Sec. III we derive the effective YSR qubit Hamiltonian in the presence of the precessing spins. In Sec. IV, we discuss how to implement coherent Rabi oscillations of the YSR qubit and provide a specific manipulation protocol. Then, in Sec. V we demonstrate that spin dynamics can be utilized for the read-out of the YSR qubit. In Sec. VI we introduce a hybrid YSR qubit – Majorana (topological) qubit that can be operated to achieve a universal set of quantum gates. We conclude with a discussion in Sec. VII.

II. MODEL HAMILTONIAN

The time-dependent Bogoliubov de Gennes (BdG) Hamiltonian describing the spin dimer system in Fig. 1 can be written in the Nambu basis

$$\Psi(\mathbf{r}) = [c_\uparrow(\mathbf{r}), c_\downarrow(\mathbf{r}), c_\downarrow^\dagger(\mathbf{r}), -c_\uparrow^\dagger(\mathbf{r})]^T \text{ as}$$

$$\begin{aligned} H_{\text{BdG}}(t) &= H_0 + \sum_{j=1,2} V_j(t) \delta(\mathbf{r} - \mathbf{R}_j), \\ H_0 &= \epsilon_p \tau_z + \Delta \tau_x, \\ V_j(t) &= J_j \mathbf{S}_j(t) \cdot \boldsymbol{\sigma}, \end{aligned} \quad (1)$$

where H_0 is the superconductor Hamiltonian and $V_j(t)$ describes the coupling of electrons to the classical spins $\mathbf{S}_j(t) = S[\sin \theta_j(t) \cos \phi_j(t), \sin \theta_j(t) \sin \phi_j(t), \cos \theta_j(t)]$ with time-dependent polar $\theta_j(t)$ and azimuthal $\phi_j(t)$ angles ($j = 1, 2$). Here, $\mathbf{R}_j = 0(\mathbf{R})$ is the position of the spin $j = 1$ ($j = 2$), J_j are the coupling strengths, $\boldsymbol{\sigma} = (\sigma_x, \sigma_y, \sigma_z)$ and $\boldsymbol{\tau} = (\tau_x, \tau_y, \tau_z)$ are the Pauli matrices in the spin and particle-hole spaces, Δ is the superconducting order parameter and $\epsilon_p = p^2/2m - \mu$ is the kinetic energy of the electrons with effective mass m , momentum p , and chemical potential μ . For simplicity, we neglect the scalar potentials [56] generated by the magnetic impurities as they do not affect directly the dynamics. The target spin \mathbf{S}_1 and test spin \mathbf{S}_2 can be addressed and driven individually through STM-ESR, and they are used for read out and manipulation, respectively.

Before proceeding with a detailed description of the dynamics, let us provide some physical insights to the spin dimer in Fig. 1 based on the recent findings in Ref. 65 concerning the dynamics of a single magnetic impurity in an s -wave SC. We first note that for the static case, the Shiba energy is given by $E_S = \Delta(1 - \alpha^2)/(1 + \alpha^2)$, with $\alpha = \pi\nu_0 JS$ and ν_0 being the density of states at the Fermi level in the normal state. For a spin precessing with frequency $\Omega \ll \Delta$ (adiabatic limit) at an angle θ around the z axis, the effective Shiba energy was found to be $E_S(\Omega) \simeq E_S - (\Omega/2) \cos \theta$, i. e. it is shifted by the Berry phase contribution. Moreover, this dynamical YSR state was found to act back on the classical spin via a *universal* torque $\boldsymbol{\tau}_S(t) = -(n_S - 1/2)F_S \dot{\mathbf{n}}(t)$, where $\mathbf{n}(t) = \mathbf{S}(t)/S$, n_S is the YSR state occupation number and F_S is the radial Berry curvature. In the absence of spin-orbit interaction, $F_S = 1/2$. This torque modifies the bare resonance frequency Ω_0 of the classical spin as $\delta\Omega/\Omega_0 \approx (1/S)(n_S - 1/2)F_S$, being a direct measurement of the occupation n_S . The energy shift (on the Shiba side) and the frequency shift (on the classical spin side) are at the core of our proposal depicted in Fig. 1: the former allows to control the bias of the double well potential by driving one of the spins, analogously to tuning the voltage-bias in double quantum dots [75], while the latter facilitates extracting the occupation of the ingap states, in analogy to quantum non-demolition qubit readouts in cavity quantum electrodynamics setups [76]. The hybridization between the two YSR states will modify the single-impurity findings, and in the following we proceed to describe in detail the dynamical YSR dimer system.

III. EFFECTIVE QUBIT HAMILTONIAN

Next we derive the low-energy Hamiltonian describing the in-gap ‘‘molecular’’ YSR states stemming from the dynamical spin dimer using a time-dependent wave function approach which will allow us to identify the effective two-level system defining the YSR qubit. The system dynamics is described by the time-dependent BdG equation $i\partial_t\psi(\mathbf{r},t) = H_{BdG}(t)\psi(\mathbf{r},t)$, where $\psi(\mathbf{r},t) = [u_\uparrow(\mathbf{r},t), u_\downarrow(\mathbf{r},t), v_\downarrow(\mathbf{r},t), -v_\uparrow(\mathbf{r},t)]^T$ is the BdG wavefunction. It is instructive to switch to the Fourier space $\psi(\mathbf{r},t) = \frac{1}{L^d} \sum_{\mathbf{k}} e^{-i\mathbf{k}\cdot\mathbf{r}} \psi(\mathbf{k},t)$ (d is the dimension of the system), which in turn allows us to write

$$\left(i\frac{\partial}{\partial t} - H_0(\mathbf{k}) \right) \psi(\mathbf{k},t) = \sum_{j=1,2} V_j(t) \psi(\mathbf{r}_j, t) e^{i\mathbf{k}\cdot\mathbf{r}_j}. \quad (2)$$

Assuming that the Shiba energies are close to the Fermi level (deep Shiba limit $\alpha_{1,2} \approx 1$) and adiabatic dynamics of the classical spins on the scale of $T_\Delta = \hbar/\Delta$, we can follow the approach described in Ref. [41, 60] to derive an effective time-dependent 8×8 Schrödinger equation that describes the dimer $i\partial_t\tilde{\psi}_i(t) = H_{ij}(t)\tilde{\psi}_j(t)$. Here, $\tilde{\psi}_{1(2)}(t) = \alpha_{1(2)}\psi(0(\mathbf{R}),t)$ is a 4-component spinor at position $r = 0$ ($r = R$) in the Nambu and spin space, while the diagonal elements $H_{11(22)}(t) \equiv H_{1(2)}(t)$ describe the interaction of SC with the spins at the positions $\mathbf{r} = 0(\mathbf{R})$

$$H_i(t) \approx -\Delta \left(\frac{\mathbf{n}_i \cdot \boldsymbol{\sigma}}{\alpha_i} + \tau_x \right) + (\mathbf{n}_i \times \dot{\mathbf{n}}_i) \cdot \boldsymbol{\sigma}, \quad (3)$$

and $H_{12}(t) = H_T(t)$ represents the tunnelling between the YSR states at different impurities

$$H_T(t) = -\Delta(\mathbf{n}_1 \cdot \boldsymbol{\sigma})(\mathbf{n}_2 \cdot \boldsymbol{\sigma})[\tilde{I}_0(R)\tau_x + \tilde{I}_1(R)\tau_z]. \quad (4)$$

Here, $\mathbf{n}_i(t) = \mathbf{S}_i(t)/S_i$ and $\tilde{I}_{0,1}(R)$ are evaluated from the overlap integrals for two impurities separated by a distance R in the superconductor (Appendix A). We point out that the time-dependence of the classical spins generates a Berry-phase contribution (the second term in Eq. (3)) that cannot be captured by only forging the effective static theory time-dependent. As shown later, while this term does not affect the qubit Hamiltonian, it does change drastically the spin expectation values at each impurity, in particular the contributions perpendicular to the instantaneous classical spin directions (which are responsible to the torques acting on the latter). This is one of the instances when an effective static theory does not suffice to describe the low-energy sector dynamics.

Let us first consider the dimer in the absence of dynamics. Projecting the above 8×8 Hamiltonian blocks, H_i and H_T , onto the low energy sector results in an effective 4×4 Hamiltonian describing the in-gap states [41, 60], (see Appendix A for details). Assuming $\theta_1 = 0$ (i. e., the first spin defines the z -axis) the in-gap energy spectrum of the 4×4 Hamiltonian becomes $|E_{1,2}| =$

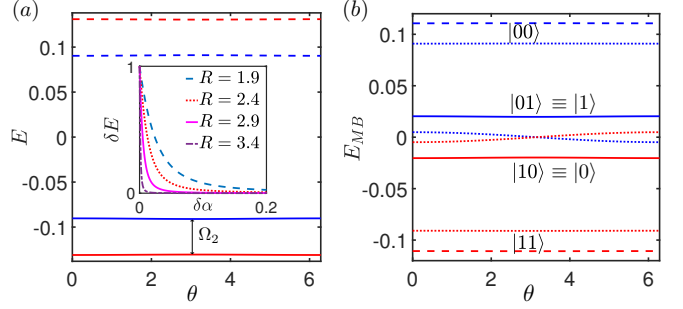


FIG. 2. (a) Single particle energy spectrum E for the in-gap states as a function of θ for $\alpha_1 = 1.15$, $\alpha_2 = 1.1$ at $R = 2.9$. Here Ω_2 is the classical spin precession frequency that matches the qubit splitting. The inset shows the energy width $\delta E = [\epsilon_q(0) - \epsilon_q(\pi)] / [\epsilon_q(0) + \epsilon_q(\pi)]$ as a function of $\delta\alpha = \alpha_1 - \alpha_2$, and for several values of R . (b) The many-body energy spectrum E_{MB} for $\alpha_1 = 1.15$, $\alpha_2 = 1.1$ and $R = 2.9$ in the absence of Coulomb interactions. The dotted lines represent the many-body energy spectrum for $\alpha_1 = \alpha_2 = 1.1$, showing a crossing at $\theta = \pi$. Here, $\{|10\rangle, |01\rangle\}$ and $\{|00\rangle, |11\rangle\}$ label the odd and even parity states, respectively, with the YSR qubit being encoded in the former. In both plots we have used $k_F = 13.55$.

$(B \pm C)/(2\alpha_1\alpha_2)$, where

$$B = \sqrt{(2\alpha_1\alpha_2 - \alpha_1 - \alpha_2)^2 + \left(t_h \cos \left(k_F R + \frac{\pi}{4} \right) \sin \frac{\theta}{2} \right)^2},$$

$$C = \sqrt{(\alpha_1 - \alpha_2)^2 + \left(t_h \sin \left(k_F R + \frac{\pi}{4} \right) \cos \frac{\theta}{2} \right)^2}, \quad (5)$$

with $t_h = 4\alpha_1\alpha_2 e^{-R}/\sqrt{2\pi k_F R}$ quantifying the tunneling strength, k_F being the Fermi momentum. Note that all energies are expressed in terms of $\Delta = 1$, while all lengths in terms of SC coherence length $\xi = v_F/\Delta$, with v_F being the Fermi velocity. In Fig. 2a, we show the corresponding energy spectrum as a function of θ . The inset of Fig. 2a depicts the relative maximum deviation in the energy difference between the lowest two energy states as a function of $\delta\alpha = \alpha_1 - \alpha_2$ for various separation distances R . From these plots, we can infer that (i) even for moderate values of $\delta\alpha$ the dependence of the energies E_i on θ is negligible and (ii) generally these energies are not equidistant. We can then encode the YSR qubit in the two lowest energy states defined by the $\{-E_1, -E_2\}$ which, for a wide range of parameters, are also well separated from the excited pair $\{E_1, E_2\}$. The qubit Hamiltonian can be written as $H_q = (\epsilon_q/2)\Sigma_z$, where $\epsilon_q \equiv \epsilon_q(\theta) = C/(2\alpha_1\alpha_2)$ is the qubit splitting, and Σ_z is the z component of the Pauli matrix acting on the states defined by $\{-E_1, -E_2\}$.

It is useful to describe the YSR qubit using a many-body states $|n_1 n_2\rangle$, where $n_{1,2} = 0, 1$ are the occupancy of the single quasi particle states. Specifically, the pair of states $\{|00\rangle, |11\rangle\}$ ($\{|01\rangle, |10\rangle\}$) span the even (odd) parity many-body states with energies $\pm|E_1 + E_2|/2$ ($\pm|E_1 - E_2|/2$). Note that within the BdG description

the two parity sectors are decoupled, and the YSR qubit defined above acts within the odd-parity states. This choice for the YSR qubit is further justified by its insensitivity to the Coulomb interaction effects that are present for double occupancy (even parity). The many-body energy spectrum depicting the odd and even parity states is shown in Fig. 2b. While the ground state corresponds to the even parity state $|1\rangle$ for the chosen parameters, the odd parity sector can be selected by tuning the offset charge with a gate voltage in the case of a finite superconducting island with a sufficiently large charging energy. Alternatively, one can utilize the spin dynamics for the initialization of the system to the odd parity state.

The many-body picture also allows us to gain further insight on the origin of the qubit states, which is determined by $\max(\delta\alpha, t_h)$. For $\delta\alpha \gg t_h$, the qubit states stem from the two individual YSR states formed under each of the impurities, while in the opposite regime $\delta\alpha \ll t_h$, they correspond to the symmetric and anti-symmetric superposition of the individual YSR states, being dictated by the tunneling. The first scenario is more advantageous as the qubit energies become insensitive to θ , as depicted in Fig. 2, rendering it more robust against fluctuations.

Having defined the YSR qubit, we can now reinstate the dynamics of the classical spins which we will exploit for the manipulation and read out of the qubit states. Without loss of generality, in the following we assume that only one spin precesses. Projecting the 4×4 time-dependent Hamiltonian onto the YSR qubit subspace, we obtain the following qubit Hamiltonian (Appendix B):

$$H_q(t) = \frac{\epsilon_q}{2} \Sigma_z + \beta(t) \cdot \Sigma, \quad (6)$$

where

$$\begin{aligned} \beta_x(t) &= t_h \frac{\sin(k_F R + \pi/4) \sin\theta \sin(\theta/2)}{4\alpha_1\alpha_2\epsilon_q} \dot{\phi}, \\ \beta_y(t) &= t_h \frac{(\alpha_1 - \alpha_2) \sin(k_F R + \pi/4) \sin(\theta/2)}{4(\alpha_1\alpha_2)^2\epsilon_q^2} \dot{\theta}, \\ \beta_z(t) &= \frac{(\alpha_2 - \alpha_1) \sin^2(\theta/2)}{2\alpha_1\alpha_2\epsilon_q} \dot{\phi}. \end{aligned} \quad (7)$$

Eqs. (6) and (7) establish the imprints of the classical spin dynamics on the effective YSR qubit Hamiltonian and represent one of our main findings. Above, we disregard the terms that act as identity in the qubit space. The first two terms in Eq. (7) induce transitions between the qubit states, while the last term allows to dynamically control the qubit splitting $\epsilon_q \rightarrow \epsilon_q + 2\beta_z(t)$. For $\delta\alpha \gg t_h$, $\beta_{x,y}(t) \propto t_h/\delta\alpha$, while $\beta_z(t) \approx \sin^2(\theta/2)\dot{\phi}/2$ is independent of any of the microscopic parameters.

IV. YSR QUBIT MANIPULATION

The YSR qubit can be manipulated by utilizing the second term in Eq. 6. The pulse sequence for introducing Rabi oscillations is shown schematically in Fig. 3a.

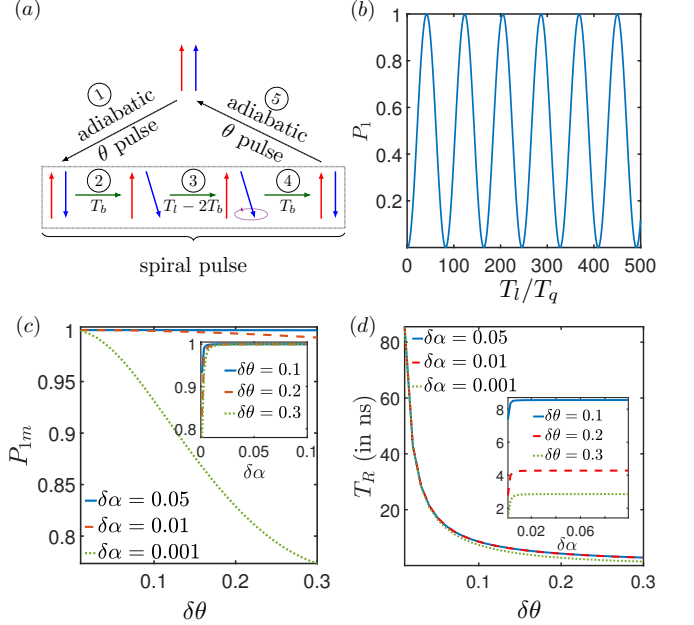


FIG. 3. (a) The pulse sequences proposal for coherent manipulation of the YSR qubit: the right spin (blue) is first rotated adiabatically from $\theta = 0$ to $\theta = \pi$ in time T_a , then driven into resonant precession with the qubit for a time T_l , after which it is rotated back adiabatically to its original orientation. The qubit can also be fully operated in the anti-parallel configuration. (b) The Rabi oscillations encoded in the probability of state $|1\rangle$ being occupied, $P_1(T_l) = |\langle 1|\psi(T_l)\rangle|^2$, as a function of the pulse time T_l for $T_a = 6T_q$ and $T_b = 0.6T_q$. The other parameters are $\delta\theta = 0.1$, $\alpha_1 = 1.15$, $\alpha_2 = 1.1$, $R = 2.9$, so that $t_h/\delta\alpha = 0.34$. (c) The Rabi oscillations amplitude, P_{1m} , as a function of the angle deviation $\delta\theta$ (main) and $\delta\alpha$ (inset). Here, $t_h/\delta\alpha = 17, 1.7, 0.34$ for $\delta\alpha = 0.001, 0.01, 0.05$, consistent with $P_{1m} \sim 1$ for $t_h \ll \delta\alpha$ on a wide range of $\delta\theta$ values. (d) The Rabi oscillation period, T_R , as a function of $\delta\theta$ (main) and $\delta\alpha$ (inset) for different values of $\delta\alpha$ and $\delta\theta$, respectively. The same conclusions as in (c) apply. All plots have been obtained using $k_F = 13.55$.

The logical states of the qubit are defined in a parallel classical spins alignment, and the resonant oscillations between the states of the qubit are induced in the anti-parallel configuration. Before describing the details of the sequence, let us underline the physical reasons for this choice. The $\beta_i(t)$ terms in Eq. (7) are much weaker for deviations $\delta\theta$ around $\theta = 0$ ($\beta_{x,z} \propto (\delta\theta)^2$ and $\beta_y \propto \delta\theta$) than when the same deviations occur in proximity of $\theta = \pi$ ($\beta_x \propto \delta\theta$ and $\beta_{y,z} \propto \text{constant}$), which makes them rather inefficient in the parallel configuration. In the idle phase, on the other hand, this is beneficial since the qubit will be more robust against random fluctuations in the angles θ and ϕ (discussed below). Nevertheless, the qubit can also be operated fully in the anti-parallel geometry, at the expense of shorter coherence times.

Let $|0\rangle$ and $|1\rangle$ be the eigenstates of the static qubit Hamiltonian at $\theta = 0$, and assume the qubit is initialized in state $|0\rangle$ at time $t = 0$. Then, at time t , the qubit state

becomes $|\psi(t)\rangle = U_q(t, 0)|0\rangle$ where the evolution operator is $U_q(t, 0) = \mathcal{T}e^{-\frac{i}{\hbar} \int_0^t dt' H_q(t')}$ with \mathcal{T} being the time-ordering operator. In step ① of the protocol in Fig. 3a, the right classical spin is rotated from parallel to the anti-parallel configuration via a pulse $\theta(t) = \pi \tanh(2\pi t/T_a)$ where T_a is the pulse length, and the evolution operator is $U_{q,1} \equiv U_q(T_a, 0)$ [77]. The amplitude of the Rabi oscillations is largest if the qubit remains in state $|0\rangle$ during this pulse. Thus, ideal results are obtained if $0-\pi$ transition is adiabatic, i.e. $T_a \gg T_q$ with $T_q = \hbar/\epsilon_q$, but almost ideal Rabi oscillations can be achieved also for fast pulses (Appendix E). In the second part of the sequence, the classical spin is driven into circular precession around the z axis so that the precession frequency Ω_2 is in resonance with the qubit splitting $\Omega_2 = \epsilon_q$. Consequently, the qubit undergoes coherent Rabi oscillations, and the evolution is described by $U_{q,2} \equiv U_q(T_a + T_l, T_a)$. In our calculations we use a spiral pulse $\phi(t) = \Omega_2 t$ and

$$\theta(t) = \pi - \delta\theta \left(\tanh \frac{t}{T_b} - \tanh \frac{t - T_l}{T_b} - 1 \right), \quad (8)$$

which first stabilizes the precession of the spin to a cone angle $\theta = \pi - \delta\theta$ in a time T_b (step ②), then causes a precession of the spin for a duration $T_l - 2T_b$ (step ③) and finally restores the classical spin back to $\theta = \pi$ in time T_b (step ④). Assuming $T_b \ll T_q$ implies that the evolution induced by $\dot{\phi}(t)$ during the ramping periods is practically frozen and we can write $U_{q,2} \approx U_{q,2g}^{-1} U_{q,2r} U_{q,2g}$, where $U_{q,2g}$ and $U_{q,2r}$ correspond to the evolution from π to $\pi - \delta\theta$ at $\dot{\phi} = 0$ and the evolution induced by the circular precession at fixed $\delta\theta$ ($\dot{\phi} = 0$) during the time $T_l - 2T_b$, respectively. Finally, the classical spin is rotated back to the parallel configuration using $U_{q,3} \equiv U_{q,1}^{-1}$ shown by step ⑤ in Fig. 3a.

The amplitude and the period of the Rabi oscillations can be determined by calculating how the probability for the qubit to be in state $|1\rangle$ after a pulse, $P_1(T_l) = |\langle 1 | \psi(T_l) \rangle|^2$ with $|\psi(T_l)\rangle = U_q(T_l)|0\rangle$, depends on the precession time T_l . We have implemented numerically the evolution operator pertaining to $U_q(t)$, and in Fig. 3b we plot $P_1(T_l)$ showing the Rabi oscillations of the qubit for the parameters $\delta\alpha = 0.05$, $\delta\theta = 0.1$, $R = 2.9$. Increasing the precession angle $\delta\theta$ increases the Rabi oscillations frequency as $\Omega_R \propto t_h \delta\theta$, but in turn reduces their amplitude, as depicted in Figs. 3c,d. The latter is a consequence of the transformation $U_{q,2g}$ which generates a finite weight $c_1 \propto (t_h/\delta\alpha)\delta\theta$ on the state $|1\rangle$ for $t_h \ll \delta\alpha$. Therefore, for a given Ω_R , the requirement for $P_{1m} \equiv \max[P_1(T_l)] \approx 1$ is $\Omega_R \ll \epsilon_q$ which, coincidentally, is similar to the adiabaticity condition in the first part of the protocol. Moreover, in the limit $T_b \ll T_q$ the transformation $U_{q,2g}$ is purely geometrical (Appendix E), and thus independent on the details of the pulse that tilts the classical spin away from the z axis by an angle $\delta\theta$. As stressed above, the manipulation can be fully performed in the anti-parallel configuration, in which case $U_q(T_l, 0) \equiv U_{q,2}$. Both the parallel and anti-parallel con-

figurations have been observed experimentally, their realization depending on the specific implementation and the distance between the impurities [68, 78].

To give some estimates for the time scale of the Rabi oscillations, let us assume $\delta\theta = 0.1$, $R = 2.9$ and $\delta\alpha = 0.05$. These rather conservative parameter values result in Rabi oscillation period $T_R \approx 8.5$ ns, which is comparable to the Rabi times observed in implementations of the Andreev qubits [17]. For the YSR qubit to be useful, the Rabi time should be much shorter than the time scales over which it loses its coherence, namely the relaxation (T_1) and pure dephasing (T_ϕ) times, which to the best of our knowledge, are largely unknown for the YSR states. Nevertheless, we can readily identify several possible sources of decoherence: (i) quasiparticle poisoning [79–81], (ii) thermal fluctuations in the magnetic moments (magnons) that define the YSR states, and (iii) phonon or photon coupling to the Shiba electrons [82]. Decoherence induced by non-equilibrium quasiparticle poisoning is highly specific to the system and thus it is difficult to provide precise scalings and estimates. Recent studies, both experimental and theoretical, show that the relaxation times pertaining to this mechanism can range from milliseconds to even seconds [79–81]. The general consensus is that their effect can be minimized by improving the samples, and it can be accounted for by a phenomenological line-width of the isolated YSR states, which in-principle can be extracted from STM-ESR measurements in the limit of weak tunnel coupling [83, 84]. The last two mechanisms, on the other hand, have not been discussed in the literature for the YSR molecule. In the following, we give a short account of the magnons-induced decoherence, while the details of the phonon (and photon) mechanism is described in Appendix F and G. The Hamiltonian describing the coupling of the qubit to the magnetization fluctuations of spins $k = 1, 2$ reads:

$$\delta H_q(t) = \sum_{k=1,2} \delta \mathbf{n}_k(t) \cdot \boldsymbol{\chi}_k \cdot \boldsymbol{\Sigma}, \quad (9)$$

with the tensor $\boldsymbol{\chi}_k \equiv [\chi_k^{\mu\nu}]$ quantifying the coupling of the two orthogonal fluctuations $\mu = 1, 2$ ($\delta \mathbf{n}_k(t) \perp \mathbf{n}_k$) of each classical spin k to the qubit Pauli matrices $\nu = x, y, z$. The elements of the tensor $\chi_k^{\mu\nu}$ can be found by projecting $\partial_{\mathbf{n}_k} H_{BdG}$ onto the qubit basis (Appendix F). Within the Bloch-Redfield framework [3], we find the following expressions for the dephasing and relaxation times, respectively:

$$\frac{1}{T_{\phi,m}} = \sum_{\mu,k=1,2} |\chi_k^{\mu z}|^2 S_{11}^k(0), \quad (10)$$

$$\frac{1}{T_{1,m}} = \sum_{\mu,\nu,k=1,2} \chi_k^{\mu\sigma} \chi_k^{\nu\bar{\sigma}} S_{\mu\nu}^k(\sigma\epsilon_q), \quad (11)$$

where $\chi_k^{\mu\sigma} = \chi_k^{\mu x} + i\sigma \chi_k^{\mu y}$ and $S_{\mu\nu}^k(\omega) = (1/2\pi) \int dt e^{-i\omega t} \langle \delta n_{k,\mu}(t) \delta n_{k,\nu}(0) \rangle$ is the noise spectrum pertaining to the fluctuations $\delta n_{k,\mu}(t)$. Above, the

$\sigma = +(-)$ terms represent the emission (absorption) rates that are related by the detailed balance condition at equilibrium. The spectrum of the fluctuations $\delta\mathbf{n}_k(t)$ is determined by the specific form of the classical spins free energy $F_S(\mathbf{n})$ and, in order to give estimates for the above decoherence times, we consider the following form (assuming the free energies of the two spins to be identical):

$$F_S(\mathbf{n}) = -\frac{\kappa}{2}n_z^2 - \gamma\mathbf{B} \cdot \mathbf{n}, \quad (12)$$

where κ measures the crystal anisotropy (intrinsic or induced by the surface), \mathbf{B} is the externally applied magnetic field, and γ the gyromagnetic ratio. Considering $\kappa > 0$, this free energy per spin is consistent with the perpendicular to the surface configurations observed in experiments. At finite temperatures $\mathbf{B} \rightarrow \mathbf{B} + \delta\mathbf{B}(t)$, with $\delta\mathbf{B}(t)$ being the stochastic contribution whose Fourier components satisfy the fluctuation-dissipation relations $\langle \delta B_\mu(\omega)\delta B_\nu(\omega') \rangle = (\alpha_g\hbar\omega)/(\gamma^2 S) [\coth(\hbar\omega/2k_B T) - 1] \delta(\omega + \omega')$ [86], where α_g and γ are the Gilbert damping and gyromagnetic coefficient, respectively. Utilizing the Landau-Lifshitz-Gilbert (LLG) equation that describes the dynamics of the classical magnets in the presence of the stochastic magnetic fields $\delta\mathbf{B}(t)$, we can evaluate the correlators $S_{\mu\nu}^k(\omega)$ in terms of $\langle \delta B_\mu(\omega)\delta B_\nu(\omega') \rangle$ (see Appendix F for more details). For simplicity, we focus only on the static (idle) parallel and anti-parallel spin configurations, assuming a spin $S = 5/2$ at each site [87, 88]. In both cases, we find that the pure dephasing rate is zero and, furthermore for $\theta = 0$, the relaxation rate is also zero, justifying quantitatively our choice for the qubit basis in the idle phase. However, at $\theta = \pi$ the longitudinal relaxation rate is non-zero, and assuming $\alpha_g = 0.001$, $\kappa = 0.1$ meV, $\alpha_1 = 1.15$, $\alpha_2 = 1.1$, $R = 2.9$ and temperature $T_0 = 100$ mK $< \epsilon_q$, we obtain $T_{1,m} \approx 3.5$ μ s [89]. Comparing that to the Rabi oscillation period we estimate that the YSR qubit can undergo a large number of Rabi oscillations before it decoheres due to magnons.

We found that both the phonon and photon couplings vanish in the anti-parallel configuration (where the YSRQ is operated), in stark contrast to the magnons which have their maximal effect. That is because both phonons and photons cannot induce spin flips, which are required for quasiparticle tunneling between the two YSR states in this configuration. In the parallel arrangement instead the phonon induced relaxation is maximal, and we evaluated it to be $T_{1,ph} \approx 5.8$ μ s. This is a slightly longer time than the coherence time induced by the noise in the magnetic moments. However, all these sources of decoherence seem to be of similar magnitude, and they are also similar to the coherence time observed in the Andreev qubits [17].

V. YSR QUBIT READ OUT

The ability to measure efficiently and fast the outcome of a computation is a prerequisite for a practical qubit. Furthermore, it allows to initialize the qubit state at the beginning of the computation. Here, we show that the qubit state can be measured using STM-ESR techniques via the torques induced by the YSR states on the classical spins. In the following, we focus on the case when the measurement is performed in the parallel spin configuration and the left spin (target) is interrogated off-resonantly with the qubit splitting as shown in Fig. 1. The former condition is considered in order to minimize the decoherence effects, while the latter allows to physically separate the manipulation and detection.

The dynamics of the left spin, \mathbf{S}_1 , is governed by the LLG equation

$$\dot{\mathbf{S}}_1 = -\gamma\mathbf{S}_1 \times \mathbf{B}(t) + \boldsymbol{\tau} + \alpha_g\mathbf{S}_1 \times \dot{\mathbf{S}}_1, \quad (13)$$

where $\boldsymbol{\tau} = -J_1\mathbf{S}_1 \times \langle \boldsymbol{\sigma}\delta(\mathbf{r}) \rangle$ is the torque pertaining to the electrons in the SC that act on spin \mathbf{S}_1 , including the YSR qubit contribution, while $\mathbf{B}(t)$ is the time-dependent external magnetic field utilized to drive the precession.

We have employed a Green function approach that describes the 8×8 Hamiltonian [60] to evaluate the total torque $\boldsymbol{\tau}_\sigma$ for the two YSR qubit states $\sigma = 0, 1$ (see Appendix C for more details). Considering \mathbf{S}_1 to precess with frequency Ω_1 in the adiabatic limit $\Omega_1 \ll \Delta$, we can write $\boldsymbol{\tau}_\sigma \approx \boldsymbol{\tau}_{\sigma s} + \boldsymbol{\tau}_{\sigma d}$, where the first term ($\boldsymbol{\tau}_{\sigma s}$) originates from the misalignment of the two classical spins, and it describes the in-gap states contribution to the RKKY interaction, while the latter ($\boldsymbol{\tau}_{\sigma d} \propto \Omega_1$) have been unravelled recently in Ref. 65 and found to have a geometrical (Berry phase) origin. In Fig. 4a we show the magnitudes of the total torque $\boldsymbol{\tau}_\sigma$, as well as the two individual contributions $\boldsymbol{\tau}_{\sigma s}$ and $\boldsymbol{\tau}_{\sigma d}$, as a function of $\delta\alpha$ for each of the two qubit states. We see that the torques are determined by the static term $\boldsymbol{\tau}_{\sigma s}$ in the limit $\Omega_1|\delta\alpha| \ll t_h^2$, while in the opposite regime, $\Omega_1|\delta\alpha| \gg t_h^2$, the dynamical contribution $\boldsymbol{\tau}_{\sigma d}$ dominates and, moreover, it reaches a universal value associated with an isolated impurity [65]. We mention that throughout the section we have neglected the effect of the bulk states on both the static and dynamical torques. In Ref. [90] it was shown that the (static) bulk contribution, which represents the conventional RKKY interaction, becomes negligible compared to that of the YSR in-gap states for separations $R \geq 1$. Furthermore, a full non-equilibrium calculation for a single impurity showed that the YSR states dominate the dynamical torque in the deep Shiba adiabatic regime and, moreover, that a finite YSR linewidth imprints onto the magnetic impurity linewidth [65], which could be utilized to measure the coherence times of the YSR qubit.

In the limit of small cone angle precession ($\theta \sim 0$), we can linearize the LLG equation, and extract the renormalized resonance frequency of spin \mathbf{S}_1 for each qubit

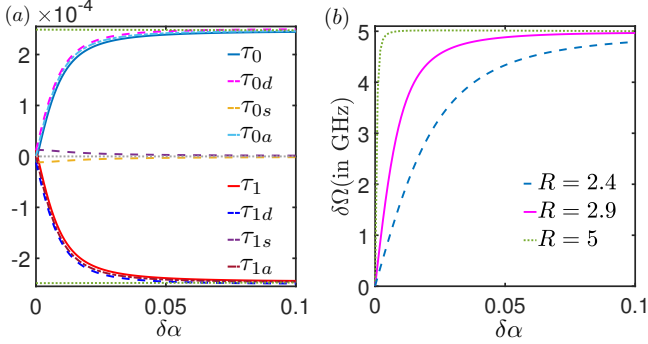


FIG. 4. (a) The total (τ_σ), static ($\tau_{\sigma s}$) and dynamic ($\tau_{\sigma d}$) torques as a function of $\delta\alpha$ for $\theta = 0.01$, $\Omega_1/\Delta = 0.1$ and $R = 2.9$. The dotted lines correspond to the asymptotic behaviour of the two contributions to the torque $\tau_{\sigma s}$ and $\tau_{\sigma d}$ for $t_h \ll \delta\alpha$. The total torque evaluated analytically ($\tau_{\sigma a}$) from Eq. (15) shows excellent agreement with the numerical result (dot-dashed lines). (b) The difference of the resonance frequency in the two qubit states, $\delta\Omega = \Omega_{r,0} - \Omega_{r,1}$, as a function of $\delta\alpha$ for $\alpha_2 = 1.1$, $\Omega_0 = 25$ GHz, and several separations $R = 2.4$, 2.9 and 5. The saturation of $\delta\Omega$ for even moderate separations indicates robust qubit detection. All plots have been obtained using $k_F = 13.55$.

state in terms of the torques as (Appendix D)

$$\Omega_{r,\sigma} = \frac{\Omega_0 - \frac{\tau'_{\sigma s}}{S}}{1 + \frac{\tau'_{\sigma d}}{S}}, \quad (14)$$

where $\tau'_{\sigma d} = (1/\Omega_1)(\partial\tau_{\sigma d}/\partial\theta)|_{\theta=0}$, $\tau'_{\sigma s} = (\partial\tau_{\sigma s}/\partial\theta)|_{\theta=0}$, and Ω_0 is the bare resonance frequency. The difference $\delta\Omega = \Omega_{r,0} - \Omega_{r,1}$ discriminates the two qubit states in STM-ESR measurements and represents one of our main findings. In Fig. 4b we plot $\delta\Omega$ as a function of $\delta\alpha$ for various distances R . For separations R such that $t_h^2 \ll \Omega_1|\delta\alpha|$, the difference $\delta\Omega$ saturates to a constant value, which we find to be $\delta\Omega \approx 8S\Omega_0/(16S^2 - 1)$ [65]. That is because the two impurities become practically decoupled, resulting in $\tau_{\sigma s} \rightarrow 0$, and only the dynamical torque from the isolated impurity contributes to the signal. We see again here that the optimal regime for operating the YSR qubit is when tunneling between the two isolated YSR states is smaller than their energy difference, in which case $\delta\Omega$ is almost invariable for wide range of system parameters.

To enrich the understanding of the above results, we present an heuristic derivation of the YSR qubit torques from basic energy considerations. In the readout regime $\dot{\theta} = 0$ and $\Omega_1 = \dot{\phi} \neq \epsilon_q$, so that the effective qubit splitting is $\epsilon_q^{\text{eff}} = \epsilon_q + 2\beta_z$ and we can neglect the $\beta_{x,y}$ terms in Eq. (7). Then, the magnitude of the torque acting on the spin S_1 by the YSR qubit in state $\sigma = 0, 1$ can be expressed as $\tau_\sigma = (-1)^\sigma \frac{1}{2} \partial_\theta \epsilon_q^{\text{eff}} \equiv (-1)^\sigma (\tau_s + \tau_d)$,

with

$$\begin{aligned} \tau_s &= -\frac{t_h^2 \sin^2(k_F R + \pi/4) \sin \theta}{2(2\alpha_1\alpha_2)^2 \epsilon_q}, \\ \tau_d &= -\Omega_1 \frac{(\alpha_2 - \alpha_1)}{4\alpha_1\alpha_2\epsilon_q} \left(\sin \theta - \frac{4\tau_s}{\epsilon_q} \sin^2(\theta/2) \right). \end{aligned} \quad (15)$$

We see that for $t_h^2 \ll \Omega_1|\delta\alpha|$ the dynamical torque dominates, reaching a universal value $\tau_d \approx (\Omega_1/4) \sin \theta$, consistent with the findings in Fig. 4a. On the other hand, for $t_h^2 \gg \Omega_1|\delta\alpha|$ the torque is controlled by the static contribution τ_s , and reaches the asymptotic value $\tau_s \approx -(t_h/4\alpha_1\alpha_2) \sin(k_F R + \pi/4) \sin(\theta/2)$ that depends strongly on the separation R between the impurities. This is again consistent with the findings in Fig. 4a. Interestingly, while for $t_h^2 \ll \Omega_1|\delta\alpha|$ the torque τ_d behaves similarly around $\theta = \pi$, for $\alpha_1 = \alpha_2 \equiv \alpha$ we obtain $\tau_s \approx -(t_h/4\alpha^2) \sin(k_F R + \pi/4)$, which is a consequence of the two qubit levels crossing each other: even though the spins are anti-parallel, a torque is exerted between the two, which is to be contrasted with the RKKY interactions mediated by the bulk [90]. This can also be interpreted as a fractional spin Josephson effect that is protected by the presence of the inversion symmetry.

To give estimates for the possible frequency shifts $\delta\Omega$, let us consider the following experimentally pertinent values: $\alpha_1 = 1.15$, $\alpha_2 = 1.1$, $R = 2.9$, $\Delta = 1$ meV ≈ 241 GHz, and $S = 5/2$. Interrogating the classical spin with frequencies $\Omega_0 \sim 25$ GHz, results in $\delta\Omega \approx 4.9$ GHz, which is well within the state-of-the-art experimental resolution [73]. Note that with the above parameters, the qubit splitting $\epsilon_q \approx 9.5$ GHz, and thus the target spin precesses off-resonantly, which is essential for the non-invasive read-out of the qubit.

VI. YSR-MAJORANA HYBRID QUBIT

The YSR qubits described here could be utilized for quantum information tasks on their own, for example, by creating a network of weakly interacting spin dimers on top of superconductors that can be addressed individually. More importantly, they could be integrated with Majorana zero modes hosted at the ends of spin chains in superconductors and exploited for performing universal quantum computation. Indeed, the braiding statistics of the Majorana zero modes alone is not sufficient for implementing a universal set of topological gate operations necessary for quantum computation, and additional non-topological gates are needed to achieve universality. A viable way to implement the missing $\pi/8$ phase gate is to control the couplings of the Majorana zero modes [91], e. g. by varying the magnetic fluxes in transmon geometries [23, 92, 93], and extremely robust geometric [94] and distillation [95] protocols can be utilized if sufficiently accurate control of the couplings is possible. However, it is not easy to realize suitable pulses to control the couplings of the Majorana modes in Shiba chains, and to

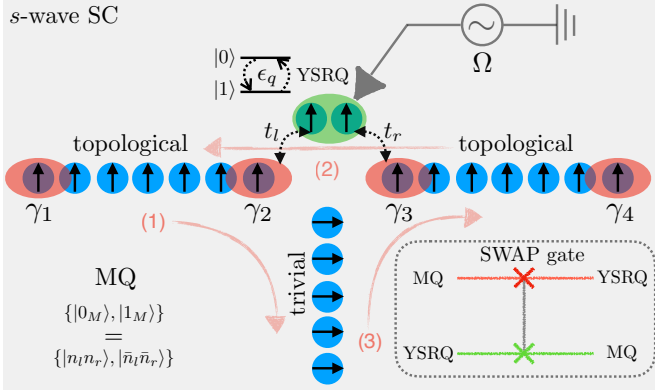


FIG. 5. Sketch of the hybrid YSR qubit (YSRQ) – Majorana qubit (MQ). The magnetic adatoms (black arrows) deposited on the top of an *s*-wave SC form three Shiba chains in a T-junction geometry. The left (*l*) and right (*r*) chains are assumed topological, hosting Majorana zero modes γ_i ($i = 1, \dots, 4$) at their ends (red) and are coupled via tunnelings $t_{l,r}$ to a spin dimer that accommodates a YSRQ (green), while the lower Shiba chain is non-topological. The states of the MQ are defined by the fermionic occupations $n_{l(r)} = 0, 1$ of the two Majorana modes on the left (right) chain, and the topologically protected Clifford gates can be implemented by braiding [steps (1), (2), and (3)] and fusing the Majorana zero modes. Driving locally the dimer rotates coherently the YSRQ (see Sec. IV), and by combining this rotation with the SWAP gates facilitated by $t_{l,r}$ (described in detail in Ref. [98]) the missing $\pi/8$ phase gate can be implemented. The SWAP gate can also be used for the measurement of the MQ via the readout of the YSRQ.

our knowledge there currently does not exist proposals for robust protocols to implement the $\pi/8$ gate in these systems. An alternative proposal to implement the $\pi/8$ gate is to integrate the Majorana zero modes with quantum dots-based qubits [24, 96–98], and here we show that this idea can be transferred to the context of the Shiba chains by utilizing the YSR qubit.

In Fig. 5 we sketch our proposal for generating a universal set of gates in a hybrid YSR qubit (YSRQ) and the Majorana qubit (MQ) system. A T-junction formed by three Shiba chains generated by magnetic impurities (or adatoms) placed on top of an *s*-wave superconductor interacts via tunnelings $t_{l,r}$ with a spin dimer that encodes a YSRQ described in the previous sections. The left and right Shiba chains are topological, hosting Majorana zero modes $\gamma_i^\dagger = \gamma_i$ ($i = 1, \dots, 4$), while the lower one is in the trivial regime. Two Majorana zero modes on the left (right) chain define a fermionic state, which can be occupied or empty. Thus, the states of the MQ can be encoded either as $\{|0_l 0_r\rangle, |1_l 1_r\rangle\}$ (in the case of even parity) or as $\{|0_l 1_r\rangle, |1_l 0_r\rangle\}$ (odd parity).

The hybrid qubit can be operated as suggested in Ref. [98]. The Clifford gates can be implemented in a topologically protected fashion by fusing Majorana zero modes and by braiding them in a T-junction shown in Fig. 5 [22]. Additionally, the non-topological $\pi/8$ gate

can be performed by first swapping the MQ state to YSRQ, then performing the $\pi/8$ gate on the YSRQ, and finally swapping the YSRQ state back onto the MQ. The SWAP gate can be constructed by utilizing the general ideas presented in Ref. [98]. The tunable couplings $t_{l,r}$ lead to an interaction Hamiltonian between the qubits

$$H_{\text{int}}(t) = \sum_{i,j=x,y,z} J_{ij}(t) \Sigma_i \mathcal{M}_j, \quad (16)$$

where \mathcal{M}_j ($j = x, y, z$) are the Pauli matrices acting on the MQ and $J_{ij}(t)$ are time-dependent coupling strengths originating from $t_{l,r} \neq 0$. In the case of $\epsilon_q = 0$ (degenerate YSRQ qubit), a specific sequence of operations for implementing the SWAP gate has been provided in Ref. [98]. In our case $\epsilon_q = 0$ can be achieved easily in the anti-parallel configuration by applying a magnetic field B_z along the z -axis. Indeed, for $\theta = \pi$ the tunneling vanishes, and we get that $\epsilon_q = 0$ at $g\mu_B B_z = 2\delta\alpha$ with g and μ_B being the g -factor and the Bohr magneton, respectively. Moreover, since we are assuming the deep Shiba limit ($\delta\alpha \ll 1$), the condition $g\mu_B B_z \ll 1$ is satisfied, which means the bulk SC remains unaffected. Alternatively, it might be possible to utilize the dynamics of the classical spin in the implementation of the SWAP gate. The SWAP gate can also be used for the initialization and measurement of the MQ via the readout of the YSRQ.

VII. DISCUSSION

In this work, we introduced and studied a novel type of quantum bit, the YSR qubit, that is encoded in the energy states of a spin dimer coupled to an *s*-wave superconductor. We have demonstrated theoretically that both the coherent manipulation and the readout of the YSR qubit can be efficiently implemented by harnessing the dynamics of the spins that engenders it. Furthermore, we scrutinized the effect of the classical spins fluctuations on the coherence of the YSR qubit, and showed robust behaviour compared to the manipulation times. Given the ability to manipulate magnetic adatoms on superconducting substrates with a high degree of control, the YSR qubit could be utilized together with Majorana topological qubits to facilitate performing universal quantum computation. We proposed one such hybrid implementation that is based on topological Shiba chains and a spin dimer hosting the YSR qubit.

There are several avenues for future studies. An immediate objective would be to generalize the time-dependent formalism described here to account for the spin-orbit effects originating from both the substrate [69] and the anisotropy of the exchange coupling between the classical spins and the superconducting electrons [68]. The spin-orbit coupling effects can provide the microscopic mechanism for the easy-axis anisotropy and therefore they are potentially useful for the operation of the YSR qubit,

but additionally they can stabilize the ferromagnetic order in adatom chains and facilitate the realization of the Majorana modes. Thus, these effects are crucial for the operation of the hybrid qubit.

Another important direction is to establish the Hamiltonian of the hybrid qubit from the microscopics in order to study the possible quantum gates and to optimally engineer the adatom deposition. Additionally, transferring coherently the information between the two types of qubits might be beneficial for entangling MQs which are separated by a large distance. The YSRQs could be entangled for example by utilizing cavity quantum electrodynamics similarly as it has been employed in various other solid-state qubits [76]. While the coupling of the YSR qubit to the magnetic field of a microwave cavity should be weak ($< \text{kHz}$), the stronger electric field component instead could couple to the qubit by affecting the tunneling t_h or via the spin-orbit coupling. Alternatively, these interactions could be ignited indirectly, via the coupling of the quantum fluctuations of the classical spins to the microwave photons [51, 99], which could also be used to drive them into precession. Moreover, such setups would naturally allow for the YSRQ to interact with other types of qubits, and enhance their functionality.

Further down the road, it would be interesting to extend the dynamical framework describing the spin dimers also to Shiba chains and 2D Shiba islands that can host Majorana end modes and chiral Majorana edges [58, 100], respectively. We believe that by triggering the magnetic

dynamics it should be possible to both manipulate and detect the Majorana edge modes, the latter by leaving their fingerprints on the STM-ESR signals. Moreover, such approaches should be advantageous as they would allow to interrogate Shiba systems with well established methods from spintronics [101]. As catalyst for another direction of future work, we speculate that the in-gap Shiba states, either in dimers or chains, could mediate out-of-equilibrium spin interactions in the presence of external magnetic drives that have no counterparts in the static situations. Given the non-perturbative nature of the coupling between the electrons in the superconductor and the spins, which converts into torques as in Eq. (15), that would require solving self-consistently the combined dynamics of the two systems. This might result in novel spin configurations that are stabilized dynamically and, on the electronic side, induce new types of (possibly dissipative) phases [102].

In conclusion, the YSR qubit proposed in this work operates well within the current experimental capabilities, and we expect to open up new possibilities for future studies on superconducting systems patterned with spins. We hope our findings will help create a roadmap towards a functional MQ in these systems.

Acknowledgments— We would like to thank Thore Posske for the interesting and fruitful discussions. The work is supported by the Foundation for Polish Science through the IRA Programme co-financed by EU within SG OP.

-
- [1] D. Vion, A. Aassime, A. Cottet, P. Joyez, H. Pothier, C. Urbina, D. Esteve, and M. H. Devoret, Manipulating the quantum state of an electrical circuit, *Science* **296**, 886 (2002).
 - [2] Y. Yu, S. Han, X. Chu, S.-I. Chu, and Z. Wang, Coherent temporal oscillations of macroscopic quantum states in a Josephson junction, *Science* **296**, 889 (2002).
 - [3] J. Koch, M. Y. Terri, J. Gambetta, A. A. Houck, D. I. Schuster, J. Majer, A. Blais, M. H. Devoret, S. M. Girvin, and R. J. Schoelkopf, Charge-insensitive qubit design derived from the Cooper pair box, *Physical Review A* **76**, 042319 (2007).
 - [4] J. Schreier, A. A. Houck, J. Koch, D. I. Schuster, B. Johnson, J. Chow, J. M. Gambetta, J. Majer, L. Frunzio, M. H. Devoret, et al., Suppressing charge noise decoherence in superconducting charge qubits, *Physical Review B* **77**, 180502 (2008).
 - [5] P. Michler, *Single Semiconductor Quantum Dots*, Vol. 28 (Springer, 2009).
 - [6] T. D. Ladd, F. Jelezko, R. Laflamme, Y. Nakamura, C. Monroe, and J. L. O’Brien, Quantum Computers, *Nature* **464**, 45 (2010).
 - [7] R. Barends, J. Kelly, A. Megrant, A. Veitia, D. Sank, E. Jeffrey, T. C. White, J. Mutus, A. G. Fowler, B. Campbell, et al., Superconducting quantum circuits at the surface code threshold for fault tolerance, *Nature* **508**, 500 (2014).
 - [8] W. Zhou and J. J. Coleman, Semiconductor Quantum Dots, *Current Opinion in Solid State and Materials Science* **20**, 352 (2016), the COSSMS Twentieth Anniversary Issue.
 - [9] C. D. Bruzewicz, J. Chiaverini, R. McConnell, and J. M. Sage, Trapped-Ion Quantum Computing: Progress and Challenges, *Applied Physics Reviews* **6**, 021314 (2019).
 - [10] F. Arute, K. Arya, R. Babbush, D. Bacon, J. C. Bardin, R. Barends, R. Biswas, S. Boixo, F. G. Brandao, D. A. Buell, et al., Quantum supremacy using a programmable superconducting processor, *Nature* **574**, 505 (2019).
 - [11] R. Aguado, A perspective on semiconductor-based superconducting qubits, *Applied Physics Letters* **117**, 240501 (2020).
 - [12] M. Kjaergaard, M. E. Schwartz, J. Braumüller, P. Krantz, J. I. J. Wang, S. Gustavsson, and W. D. Oliver, Superconducting qubits: Current state of play, *Annual Review of Condensed Matter Physics* **11**, 369 (2020).
 - [13] H.-S. Zhong, H. Wang, Y.-H. Deng, M.-C. Chen, L.-C. Peng, Y.-H. Luo, J. Qin, D. Wu, X. Ding, Y. Hu, et al., Quantum computational advantage using photons, *Science* **370**, 1460 (2020).
 - [14] F. Pan and P. Zhang, Simulating the Sycamore quantum supremacy circuits, *arXiv:2103.03074* (2021).
 - [15] N. M. Chtchelkatchev and Y. V. Nazarov, Andreev quantum dots for spin manipulation, *Physical Review Letters* **90**, 226806 (2003).
 - [16] A. Zazunov, V. Shumeiko, E. Bratus, J. Lantz, and G. Wendin, Andreev level qubit, *Physical Review Letters*

- 90**, 087003 (2003).
- [17] C. Janvier, L. Tosi, L. Bretheau, Q. Girit, M. Stern, P. Bertet, P. Joyez, D. Vion, D. Esteve, M. Goffman, et al., Coherent manipulation of Andreev states in superconducting atomic contacts, *Science* **349**, 1199 (2015).
- [18] S. Park and A. L. Yeyati, Andreev spin qubits in multi-channel Rashba nanowires, *Physical Review B* **96**, 125416 (2017).
- [19] L. Tosi, C. Metzger, M. Goffman, C. Urbina, H. Pothier, S. Park, A. L. Yeyati, J. Nygård, and P. Krogstrup, Spin-orbit splitting of Andreev states revealed by microwave spectroscopy, *Physical Review X* **9**, 011010 (2019).
- [20] M. Hays, V. Fatemi, D. Bouman, J. Cerrillo, S. Diamond, K. Serniak, T. Connolly, P. Krogstrup, J. Nygård, A. L. Yeyati, et al., Coherent manipulation of an Andreev spin qubit, [arXiv:2101.06701](https://arxiv.org/abs/2101.06701) (2021).
- [21] J. Cerrillo, M. Hays, V. Fatemi, and A. L. Yeyati, Spin coherent manipulation in Josephson weak links, *Physical Review Research* **3**, L022012 (2021).
- [22] J. Alicea, Y. Oreg, G. Refael, F. von Oppen, and M. P. A. Fisher, Non-Abelian statistics and topological quantum information processing in 1D wire networks, *Nature Physics* **7**, 412 (2011).
- [23] T. Hyart, B. van Heck, I. C. Fulga, M. Burrello, A. R. Akhmerov, and C. W. J. Beenakker, Flux-controlled quantum computation with Majorana fermions, *Physical Review B* **88**, 035121 (2013).
- [24] D. Aasen, M. Hell, R. V. Mishmash, A. Higginbotham, J. Danon, M. Leijnse, T. S. Jespersen, J. A. Folk, C. M. Marcus, K. Flensberg, and J. Alicea, Milestones Toward Majorana-Based Quantum Computing, *Physical Review X* **6**, 031016 (2016).
- [25] T. Karzig, C. Knapp, R. M. Lutchyn, P. Bonderson, M. B. Hastings, C. Nayak, J. Alicea, K. Flensberg, S. Plagge, Y. Oreg, C. M. Marcus, and M. H. Freedman, Scalable designs for quasiparticle-poisoning-protected topological quantum computation with Majorana zero modes, *Physical Review B* **95**, 235305 (2017).
- [26] C. W. J. Beenakker, Search for non-Abelian Majorana braiding statistics in superconductors, *SciPost Phys. Lect. Notes* , 15 (2020).
- [27] K. Flensberg, F. von Oppen, and A. Stern, Engineered platforms for topological superconductivity and Majorana zero modes, [arXiv:2103.05548](https://arxiv.org/abs/2103.05548).
- [28] L. Yu, Bound state in superconductors with paramagnetic impurities, *Acta Phys. Sin* **21**, 75 (1965).
- [29] H. Shiba, Classical spins in superconductors, *Progress of theoretical Physics* **40**, 435 (1968).
- [30] A. Rusinov, Superconductivity near a paramagnetic impurity, *Soviet Journal of Experimental and Theoretical Physics Letters* **9**, 85 (1969).
- [31] W. Bauriedl, P. Ziemann, and W. Buckel, Electron-tunneling observation of impurity bands in superconducting manganese-implanted lead, *Physical Review Letters* **47**, 1163 (1981).
- [32] G. C. Ménard, S. Guissart, C. Brun, S. Pons, V. S. Stolyarov, F. Debontridder, M. V. Leclerc, E. Janod, L. Cario, D. Roditchev, et al., Coherent long-range magnetic bound states in a superconductor, *Nature Physics* **11**, 1013 (2015).
- [33] B. W. Heinrich, J. I. Pascual, and K. J. Franke, Single magnetic adsorbates on s-wave superconductors, *Progress in Surface Science* **93**, 1 (2018).
- [34] D. Wang, J. Wiebe, R. Zhong, G. Gu, and R. Wiesen-
danger, Spin-Polarized Yu-Shiba-Rusinov States in an Iron-Based Superconductor, *Physical Review Letters* **126**, 076802 (2021).
- [35] T.-P. Choy, J. Edge, A. Akhmerov, and C. Beenakker, Majorana fermions emerging from magnetic nanoparticles on a superconductor without spin-orbit coupling, *Physical Review B* **84**, 195442 (2011).
- [36] S. Nakosai, Y. Tanaka, and N. Nagaosa, Two-dimensional p-wave superconducting states with magnetic moments on a conventional s-wave superconductor, *Physical Review B* **88**, 180503 (2013).
- [37] S. Nadj-Perge, I. Drozdov, B. A. Bernevig, and A. Yazdani, Proposal for realizing Majorana fermions in chains of magnetic atoms on a superconductor, *Physical Review B* **88**, 020407 (2013).
- [38] B. Braunecker and P. Simon, Interplay between classical magnetic moments and superconductivity in quantum one-dimensional conductors: toward a self-sustained topological Majorana phase, *Physical Review Letters* **111**, 147202 (2013).
- [39] J. Klinovaja, P. Stano, A. Yazdani, and D. Loss, Topological superconductivity and Majorana fermions in RKKY systems, *Physical Review Letters* **111**, 186805 (2013).
- [40] M. Vazifeh and M. Franz, Self-organized topological state with Majorana fermions, *Physical Review Letters* **111**, 206802 (2013).
- [41] F. Pientka, L. I. Glazman, and F. von Oppen, Topological superconducting phase in helical Shiba chains, *Physical Review B* **88**, 155420 (2013).
- [42] S. Nadj-Perge, I. K. Drozdov, J. Li, H. Chen, S. Jeon, J. Seo, A. H. MacDonald, B. A. Bernevig, and A. Yazdani, Observation of Majorana fermions in ferromagnetic atomic chains on a superconductor, *Science* **346**, 602 (2014).
- [43] F. Pientka, L. I. Glazman, and F. von Oppen, Unconventional topological phase transitions in helical Shiba chains, *Physical Review B* **89**, 180505 (2014).
- [44] K. Pöyhönen, A. Westström, J. Röntynen, and T. Ojanen, Majorana states in helical Shiba chains and ladders, *Physical Review B* **89**, 115109 (2014).
- [45] A. Heimes, P. Kotetes, and G. Schön, Majorana fermions from Shiba states in an antiferromagnetic chain on top of a superconductor, *Physical Review B* **90**, 060507 (2014).
- [46] I. Reis, D. Marchand, and M. Franz, Self-organized topological state in a magnetic chain on the surface of a superconductor, *Physical Review B* **90**, 085124 (2014).
- [47] A. Westström, K. Pöyhönen, and T. Ojanen, Topological properties of helical Shiba chains with general impurity strength and hybridization, *Physical Review B* **91**, 064502 (2015).
- [48] Y. Peng, F. Pientka, L. I. Glazman, and F. von Oppen, Strong localization of Majorana end states in chains of magnetic adatoms, *Physical Review Letters* **114**, 106801 (2015).
- [49] J. Röntynen and T. Ojanen, Topological superconductivity and high Chern numbers in 2D ferromagnetic Shiba lattices, *Physical Review Letters* **114**, 236803 (2015).
- [50] B. Braunecker and P. Simon, Self-stabilizing temperature-driven crossover between topological and nontopological ordered phases in one-dimensional conductors, *Physical Review B* **92**, 241410 (2015).
- [51] J. Zhang, Y. Kim, E. Rossi, and R. M. Lutchyn, Topological superconductivity in a multichannel Yu-Shiba-Rusinov chain, *Physical Review B* **93**, 024507 (2016).
- [52] S. Hoffman, J. Klinovaja, and D. Loss, Topological phases

- of inhomogeneous superconductivity, *Physical Review B* **93**, 165418 (2016).
- [53] L. Kimme and T. Hyart, Existence of zero-energy impurity states in different classes of topological insulators and superconductors and their relation to topological phase transitions, *Physical Review B* **93**, 035134 (2016).
- [54] T. Neupert, A. Yazdani, and B. A. Bernevig, Shiba chains of scalar impurities on unconventional superconductors, *Physical Review B* **93**, 094508 (2016).
- [55] G. M. Andolina and P. Simon, Topological properties of chains of magnetic impurities on a superconducting substrate: Interplay between the Shiba band and ferromagnetic wire limits, *Physical Review B* **96**, 235411 (2017).
- [56] L. Schneider, P. Beck, T. Posske, D. Crawford, E. Mascot, S. Rachel, R. Wiesendanger, and J. Wiebe, Topological Shiba bands in artificial spin chains on superconductors, *Nature Physics* **1** (2021).
- [57] L. Schneider, P. Beck, J. Neuhaus-Steinmetz, T. Posske, J. Wiebe, and R. Wiesendanger, Controlled length-dependent interaction of Majorana modes in Yu-Shiba-Rusinov chains, [arXiv:2104.11503](#) (2021).
- [58] S. Kezilebieke, M. N. Huda, V. Vaňo, M. Aapro, S. C. Ganguli, O. J. Silveira, S. Głodzik, A. S. Foster, T. Ojanen, and P. Liljeroth, Topological superconductivity in a van der Waals heterostructure, *Nature* **588**, 424 (2020).
- [59] V. Kaladzhyan, C. Bena, and P. Simon, Asymptotic behavior of impurity-induced bound states in low-dimensional topological superconductors, *Journal of Physics: Condensed Matter* **28**, 485701 (2016).
- [60] V. Kaladzhyan, P. Simon, and M. Trif, Controlling topological superconductivity by magnetization dynamics, *Physical Review B* **96**, 020507 (2017).
- [61] K. Akkaravarawong, J. I. Väyrynen, J. D. Sau, E. A. Demler, L. I. Glazman, and N. Y. Yao, Probing and dressing magnetic impurities in a superconductor, *Phys. Rev. Research* **1**, 033091 (2019).
- [62] J. Li, T. Neupert, B. A. Bernevig, and A. Yazdani, Manipulating majorana zero modes on atomic rings with an external magnetic field, *Nature Communications* **7**, 10395 (2016).
- [63] A. Kreisel, T. Hyart, and B. Rosenow, Tunable topological states hosted by unconventional superconductors with adatoms, [arXiv:2102.12502](#) [cond-mat.supr-con].
- [64] S. Karan, H. Huang, C. Padurariu, B. Kubala, G. Morra, A. L. Yeyati, J. C. Cuevas, J. Ankerhold, K. Kern, and C. R. Ast, Superconducting quantum interference at the atomic scale, [arXiv:2102.12521](#) [cond-mat.supr-con].
- [65] A. Mishra, S. Takei, P. Simon, and M. Trif, Dynamical torque from Shiba states in *s*-wave superconductors, *Physical Review B* **103**, L121401 (2021).
- [66] S. Kezilebieke, M. Dvorak, T. Ojanen, and P. Liljeroth, Coupled Yu–Shiba–Rusinov states in molecular dimers on NbSe₂, *Nano letters* **18**, 2311 (2018).
- [67] M. Ruby, B. W. Heinrich, Y. Peng, F. von Oppen, and K. J. Franke, Wave-Function Hybridization in Yu-Shiba-Rusinov Dimers, *Physical Review Letters* **120**, 156803 (2018).
- [68] H. Ding, Y. Hu, M. T. Randeria, S. Hoffman, O. Deb, J. Klinovaja, D. Loss, and A. Yazdani, Tuning interactions between spins in a superconductor, *Proceedings of the National Academy of Sciences* **118** (2021).
- [69] P. Beck, L. Schneider, L. Rózsa, K. Palotás, A. Lászlóffy, L. Szunyogh, J. Wiebe, and R. Wiesendanger, Spin-orbit coupling induced splitting of Yu-Shiba-Rusinov states in antiferromagnetic dimers, *Nature Communications* **12**, 1 (2021).
- [70] A. V. Balatsky, M. Nishijima, and Y. Manassen, Electron spin resonance-scanning tunneling microscopy, *Advances in Physics* **61**, 117 (2012).
- [71] F. D. Natterer, K. Yang, W. Paul, P. Willke, T. Choi, T. Greber, A. J. Heinrich, and C. P. Lutz, Reading and writing single-atom magnets, *Nature* **543**, 226 (2017).
- [72] P. Willke, W. Paul, F. D. Natterer, K. Yang, Y. Bae, T. Choi, J. Fernández-Rossier, A. J. Heinrich, and C. P. Lutz, Probing quantum coherence in single-atom electron spin resonance, *Science advances* **4**, eaaq1543 (2018).
- [73] K. Yang, W. Paul, F. D. Natterer, J. L. Lado, Y. Bae, P. Willke, T. Choi, A. Ferrón, J. Fernández-Rossier, A. J. Heinrich, and C. P. Lutz, Tuning the Exchange Bias on a Single Atom from 1 mT to 10 T, *Physical Review Letters* **122**, 227203 (2019).
- [74] W. M. van Weerenburg, M. Steinbrecher, N. P. van Mullekom, J. W. Gerritsen, H. von Allwörden, F. D. Natterer, and A. A. Khajetorians, A scanning tunneling microscope capable of electron spin resonance and pump-probe spectroscopy at mK temperature and in vector magnetic field, *Review of Scientific Instruments* **92**, 033906 (2021).
- [75] R. Hanson, L. P. Kouwenhoven, J. R. Petta, S. Tarucha, and L. M. K. Vandersypen, Spins in few-electron quantum Dots, *Rev. Mod. Phys.* **79**, 1217 (2007).
- [76] Burkard, Guido and Gullans, Michael J. and Mi, Xiao and Petta, Jason R., Superconductor-semiconductor hybrid-circuit quantum electrodynamics, *Nature Reviews Physics* **2**, 129 (2020).
- [77] I. D. Mayergoyz, G. Bertotti, and C. Serpico, *Nonlinear magnetization dynamics in nanosystems* (Elsevier, 2009).
- [78] D.-J. Choi, C. G. Fernández, E. Herrera, C. Rubio-Verdú, M. M. Ugeda, I. Guillamón, H. Suderow, J. I. Pasqual, and N. Lorente, Influence of Magnetic Ordering between Cr Adatoms on the Yu-Shiba-Rusinov States of the β -Bi₂Pd Superconductor, *Physical Review Letters* **120**, 167001 (2018).
- [79] J. van Veen, A. Proutski, T. Karzig, D. I. Pikulin, R. M. Lutchyn, J. Nygård, P. Krogstrup, A. Geresdi, L. P. Kouwenhoven, and J. D. Watson, Magnetic-field-dependent quasiparticle dynamics of nanowire single-Cooper-pair transistors, *Physical Review B* **98**, 174502 (2018).
- [80] E. T. Mannila, P. Samuelsson, S. Simbierowicz, J. T. Peltonen, V. Vesterinen, L. Grönberg, J. Hassel, V. F. Maisi, and J. P. Pekola, A superconductor free of quasiparticles for seconds, [arXiv:2102.00484](#) [cond-mat.supr-con].
- [81] T. Karzig, W. S. Cole, and D. I. Pikulin, Quasiparticle Poisoning of Majorana Qubits, *Physical Review Letters* **126**, 057702 (2021).
- [82] M. Ruby, F. Pientka, Y. Peng, F. von Oppen, B. W. Heinrich, and K. J. Franke, End states and subgap structure in proximity-coupled chains of magnetic adatoms, *Physical Review Letters* **115**, 197204 (2015).
- [83] H. Huang, C. Padurariu, J. Senkpiel, R. Drost, A. L. Yeyati, J. C. Cuevas, B. Kubala, J. Ankerhold, K. Kern, and C. R. Ast, Tunnelling dynamics between superconducting bound states at the atomic limit, *Nature Physics*

- , 1 (2020).
- [84] H. Huang, J. Senkpiel, C. Padurariu, R. Drost, A. Vil-las, R. L. Klees, A. L. Yeyati, J. C. Cuevas, B. Kubala, J. Ankerhold, K. Kern, and C. R. Ast, Spin-dependent tunnelling between individual superconducting bound states, *Physical Review Research* **3**, L032008 (2021).
- [3] K. Blum, *Density matrix theory and applications*, Vol. 64 (Springer Science & Business Media, 2012).
- [86] L. D. Landau and E. M. Lifshitz, *Course of theoretical physics* (Elsevier, 2013).
- [87] R. Žitko, Quantum impurity models for magnetic adsorbates on superconductor surfaces, *PhyB* **536**, 230 (2018).
- [88] F. von Oppen and K. J. Franke, Yu-Shiba-Rusinov states in real metals, *Phys. Rev. B* **103**, 205424 (2021).
- [89] N. Hatter, B. W. Heinrich, D. Rolf, and K. J. Franke, Scaling of Yu-Shiba-Rusinov energies in the weak-coupling Kondo regime, *Nature Communications* **8**, 1 (2017).
- [90] N. Y. Yao, L. I. Glazman, E. A. Demler, M. D. Lukin, and J. D. Sau, Enhanced Antiferromagnetic Exchange between Magnetic Impurities in a Superconducting Host, *Physical Review Letters* **113**, 087202 (2014).
- [91] S. Bravyi, Universal quantum computation with the $\nu = 5/2$ fractional quantum Hall State, *Physical Review A* **73**, 042313 (2006).
- [92] F. Hassler, A. R. Akhmerov, and C. W. J. Beenakker, The top-transmon: a hybrid superconducting qubit for parity-protected quantum computation, *New Journal of Physics* **13**, 095004 (2011).
- [93] B. van Heck, T. Hyart, and C. W. J. Beenakker, Minimal circuit for a flux-controlled Majorana qubit in a quantum spin-Hall insulator, *Physica Scripta* **T164**, 014007 (2015).
- [94] T. Karzig, Y. Oreg, G. Refael, and M. H. Freedman, Universal Geometric Path to a Robust Majorana Magic Gate, *Phys. Rev. X* **6**, 031019 (2016).
- [95] S. Bravyi and A. Kitaev, Universal quantum computation with ideal Clifford gates and noisy ancillas, *Phys. Rev. A* **71**, 022316 (2005).
- [96] K. Flensberg, Non-Abelian operations on Majorana fermions via single-charge control, *Physical review letters* **106**, 090503 (2011).
- [97] M. Leijnse and K. Flensberg, Quantum Information Transfer between Topological and Spin Qubit Systems, *Physical Review Letters* **107**, 210502 (2011).
- [98] S. Hoffman, C. Schrade, J. Klinovaja, and D. Loss, Universal quantum computation with hybrid spin-Majorana qubits, *Physical Review B* **94**, 045316 (2016).
- [99] Y. Tabuchi, S. Ishino, T. Ishikawa, R. Yamazaki, K. Usami, and Y. Nakamura, Hybridizing Ferromagnetic Magnons and Microwave Photons in the Quantum Limit, *Physical Review Letters* **113**, 083603 (2014).
- [100] G. C. MÅ©nard, S. Guissart, C. Brun, R. T. Leriche, M. Trif, F. Debontridder, D. Demaille, D. Roditchev, P. Simon, and T. Cren, Two-dimensional topological superconductivity in Pb/Co/Si(111), *Nature Communications* **8**, 2040 (2017).
- [101] J. Sinova, S. O. Valenzuela, J. Wunderlich, C. H. Back, and T. Jungwirth, Spin Hall effects, *Rev. Mod. Phys.* **87**, 1213 (2015).
- [102] S. Ghosh, F. Freimuth, O. Gomonay, S. Blügel, and Y. Mokrousov, Driving spin chirality by electron dynamics in laser-excited antiferromagnets, [arXiv:2011.01670 \[cond-mat.mes-hall\]](https://arxiv.org/abs/2011.01670).

Appendix A: Derivation of the low-energy Hamiltonian

In this section, we show the derivation of the Hamiltonian describing the YSR qubit given by Eq. (6). The total SC Hamiltonian written in the Nambu basis $\Psi(\mathbf{r}) = [c_\uparrow(\mathbf{r}), c_\downarrow(\mathbf{r}), c_\downarrow^\dagger(\mathbf{r}), -c_\uparrow^\dagger(\mathbf{r})]^T$ reads

$$H_{\text{tot}}(t) = \frac{1}{2} \int d\mathbf{r} \Psi^\dagger(\mathbf{r}) H_{\text{BdG}}(t) \Psi(\mathbf{r}), \quad (\text{A1})$$

where, as described in the main text [Eq. (1)], the BdG Hamiltonian is

$$H_{\text{BdG}}(t) = H_0 + \sum_{j=1,2} V_j(t) \delta(\mathbf{r} - \mathbf{R}_j), \quad (\text{A2})$$

$$\begin{aligned} H_0 &= \epsilon_p \tau_z + \Delta \tau_x, \\ V_j(t) &= J_j \mathbf{S}_j(t) \cdot \boldsymbol{\sigma}, \end{aligned} \quad (\text{A3})$$

while $\mathbf{S}_i(t) = S(\sin \theta_i \cos \phi_i, \sin \theta_i \sin \phi_i, \cos \theta_i)$, with θ_i and ϕ_i being the (time-dependent) polar and azimuthal angles for spin $i = 1, 2$. The time dependent Schrodinger equation can be written as $i\partial_t \psi(\mathbf{r}, t) = H_{\text{BdG}} \psi(\mathbf{r}, t)$. By using the Fourier decomposition $\psi(\mathbf{r}, t) = \frac{1}{L^d} \sum_{\mathbf{k}} e^{-i\mathbf{k} \cdot \mathbf{r}} \psi(\mathbf{k}, t)$, we can recast the BdG equation in the following form:

$$\left(i \frac{\partial}{\partial t} - H_0(\mathbf{k}) \right) \psi(\mathbf{k}, t) = \sum_{j=1,2} V_j(t) \psi(\mathbf{r}_j, t) e^{i\mathbf{k} \cdot \mathbf{r}_j}, \quad (\text{A4})$$

which, in the static limit pertains to the substitution $i\partial_t \rightarrow E$ and coincides with the equation for the spectrum presented in Ref. [41]. In the frequency domain, and retaining only the leading order terms in ω , we obtain:

$$\psi(\mathbf{r}_i, \omega) \approx - \sum_{j=1,2} [(\omega + \Delta \tau_x) I_0(\mathbf{r}_j - \mathbf{r}_i) + I_1(\mathbf{r}_j - \mathbf{r}_i) \tau_z] \int d\omega' V_j(\omega') \psi(\mathbf{r}_j, \omega - \omega') e^{i\mathbf{k} \cdot \mathbf{r}_j}, \quad (\text{A5})$$

where

$$I_0(\mathbf{r}) \equiv I_0(r) = \int \frac{d\mathbf{k}}{(2\pi)^d} \frac{e^{i\mathbf{k} \cdot \mathbf{r}}}{\epsilon_k^2 + \Delta^2}; \quad I_1(\mathbf{r}) \equiv I_1(r) = \int \frac{d\mathbf{k}}{(2\pi)^d} \frac{\epsilon_k e^{i\mathbf{k} \cdot \mathbf{r}}}{\epsilon_k^2 + \Delta^2}. \quad (\text{A6})$$

In the above expressions, we retained only the leading order corrections in ω , assuming that the time dynamics of the classical spins as well as that of the emerging Shiba energies is such that $\omega \ll \Delta$ (adiabatic regime). For a 2D superconductor the integrals $I_{0,1}(r)$ can be written as $I_0(r) = (2\nu_0/\Delta) \tilde{I}_0(r)$ and $I_1(r) = 2\nu_0 \tilde{I}_1(r)$ [41], where

$$\tilde{I}_{0(1)}(r) = \text{Im}(\text{Re}) K_0 \left[-i \left(1 + i \frac{\Delta}{v_F k_F} \right) k_F r \right], \quad (\text{A7})$$

ν_0 is the density of states, k_F the Fermi momentum, v_F the Fermi velocity and K_0 is the modified Bessel function of second kind. At $r = 0$ they give $\tilde{I}_0 = \pi/2$ and $\tilde{I}_1 = 0$, while for $k_F r \gg 1$ (a limit utilized throughout our work) the asymptotic expressions are [60]

$$\tilde{I}_0(r) \approx \sqrt{\frac{2}{\pi}} \frac{\sin(k_F r + \pi/4)}{\sqrt{k_F r}} e^{-\Delta r/v_F}, \quad \tilde{I}_1(r) \approx \sqrt{\frac{2}{\pi}} \frac{\cos(k_F r + \pi/4)}{\sqrt{k_F r}} e^{-\Delta r/v_F}. \quad (\text{A8})$$

Next, we switch back to the time-domain, and we get

$$\psi(\mathbf{r}_i, t) \approx - \sum_{j=1,2} [(i\partial_t + \Delta \tau_x) \tilde{I}_0(\mathbf{r}_j - \mathbf{r}_i) + \tilde{I}_1(\mathbf{r}_j - \mathbf{r}_i) \tau_z] V_j(t) \psi(\mathbf{r}_j, t). \quad (\text{A9})$$

Defining $\tilde{\psi}(\mathbf{r}_i, t) = \alpha_i \psi(\mathbf{r}_i, t)$, we can manipulate further this expression by writing the combined evolution as:

$$i \frac{\partial}{\partial t} \begin{pmatrix} \tilde{\psi}(\mathbf{r}_1, t) \\ \tilde{\psi}(\mathbf{r}_2, t) \end{pmatrix} = \begin{pmatrix} H_1(t) & H_T(t) \\ H_T^\dagger(t) & H_2(t) \end{pmatrix} \begin{pmatrix} \tilde{\psi}(\mathbf{r}_1, t) \\ \tilde{\psi}(\mathbf{r}_2, t) \end{pmatrix}, \quad (\text{A10})$$

where

$$\begin{aligned} H_i(t) &= -\Delta \left(\frac{\mathbf{n}_i \cdot \boldsymbol{\sigma}}{\alpha_i} + \tau_x \right) + (\mathbf{n}_i \times \dot{\mathbf{n}}_i) \cdot \boldsymbol{\sigma}, \\ H_T(t) &= -\Delta(\mathbf{n}_1 \cdot \boldsymbol{\sigma})(\mathbf{n}_2 \cdot \boldsymbol{\sigma})[\tilde{I}_0(R)\tau_x + \tilde{I}_1(R)\tau_z], \end{aligned} \quad (\text{A11})$$

and $\mathbf{n}_i \equiv \mathbf{n}_i(t) = \mathbf{S}_i(t)/S_i$. As mentioned in the main text, the dynamics of the spins induce an extra term in the local Hamiltonian matrix element of Berry phase origin. Without this term, the transverse spin expectation values at the positions of the impurities would have the wrong sign.

To help distinguish the low and high energy sectors, which in turn will allow us to eliminate perturbatively the terms that couple them, it is instructive to perform first a unitary transformation $U_0 = \exp(i\pi\tau_y/4)$ that converts $\tau_x \leftrightarrow \tau_z$, followed by a (time-dependent) $U_i(t) = \tau_0 \otimes \tilde{U}_i(t)$ that acts on site $i = 0(R)$ and diagonalizes the terms $\propto \mathbf{n}_i \cdot \boldsymbol{\sigma}$:

$$\tilde{U}_i(t) = \begin{pmatrix} \cos \theta_i/2 & \sin \theta_i/2 \\ e^{i\phi_i} \sin \theta_i/2 & -e^{i\phi_i} \cos \theta_i/2 \end{pmatrix}. \quad (\text{A12})$$

These rotations affect the terms in Eq. (A11) and they become:

$$\begin{aligned} \tilde{H}_i(t) &= \tilde{U}_i^\dagger H_i(t) \tilde{U}_i - i\tilde{U}_i^\dagger \dot{\tilde{U}}_i = -\Delta \left(\frac{1}{\alpha_i} \sigma_z + \tau_z \right) + \frac{\dot{\phi}_i}{2} (1 - \cos \theta_i \sigma_z + \sin \theta_i \sigma_x) - \frac{\dot{\theta}_i}{2} \sigma_y, \\ \tilde{H}_T(t) &= \tilde{U}_1^\dagger H_T(t) \tilde{U}_2 = -\Delta U_1^\dagger(\mathbf{n}_1 \cdot \boldsymbol{\sigma})(\mathbf{n}_2 \cdot \boldsymbol{\sigma}) U_2 [\tilde{I}_0(R)\tau_z - \tilde{I}_1(R)\tau_x]. \end{aligned} \quad (\text{A13})$$

The low (high) 4×4 energy sector is spanned by the $\sigma_z \tau_z = -1(1)$ and the corresponding energies of the isolated Shiba states are $\pm\Delta(1 - 1/\alpha_i)$ [$\pm\Delta(1 + 1/\alpha_i)$]. Consequently, we can then project the remaining terms, i. e., the tunneling and the velocity contributions $\propto \dot{\phi}_i, \dot{\theta}_i$, onto the low-energy sector to obtain an effective time-dependent Hamiltonian.

To simplify the discussion, from here onward, we assume the left spin (1) is static and aligned along the z -direction, or $\theta_1, \phi_1 = 0$, and that $\theta_2 \equiv \theta$ and $\phi_2 \equiv \phi$. Furthermore, we also consider that all lengths are expressed in terms of $\xi_{SC} = v_F/\Delta$, and set $\Delta = 1$. Then, the projected 4×4 low-energy Hamiltonian can be written as

$$H_l(t) \equiv \mathcal{P}_l \tilde{H}(t) \mathcal{P}_l = H_{l,0}(t) + \dot{\phi} A_{l,\phi}(t) + \dot{\theta} A_{l,\theta}(t), \quad (\text{A14})$$

where \mathcal{P}_l is the corresponding projector while

$$H_{l,0}(t) = \begin{bmatrix} -1 + \frac{1}{\alpha_1} & 0 & -\frac{e^{-R+i\phi} \cos(\theta/2) \sin(k_F R + \pi/4)}{\sqrt{\pi k_F R/2}} & \frac{e^{-R+i\phi} \sin(\theta/2) \cos(k_F R + \pi/4)}{\sqrt{\pi k_F R/2}} \\ 0 & 1 - \frac{1}{\alpha_1} & -\frac{e^{-R} \sin(\theta/2) \cos(k_F R + \pi/4)}{\sqrt{\pi k_F R/2}} & \frac{e^{-R} \cos(\theta/2) \sin(k_F R + \pi/4)}{\sqrt{\pi k_F R/2}} \\ -\frac{e^{-R-i\phi} \cos(\theta/2) \sin(k_F R + \pi/4)}{\sqrt{\pi k_F R/2}} & -\frac{e^{-R} \sin(\theta/2) \cos(k_F R + \pi/4)}{\sqrt{\pi k_F R/2}} & -1 + \frac{1}{\alpha_2} & 0 \\ \frac{e^{-R-i\phi} \sin(\theta/2) \cos(k_F R + \pi/4)}{\sqrt{\pi k_F R/2}} & \frac{e^{-R} \cos(\theta/2) \sin(k_F R + \pi/4)}{\sqrt{\pi k_F R/2}} & 0 & 1 - \frac{1}{\alpha_2} \end{bmatrix}, \quad (\text{A15})$$

represents the instantaneous projected Hamiltonian, with $A_{l,\phi}(t)$ and $A_{l,\theta}(t)$ being the projected gauge field terms associated with the $\dot{\phi}$ and $\dot{\theta}$ contributions in Eq. (A14).

Appendix B: Effective qubit Hamiltonian

We can further diagonalize the instantaneous 4×4 Hamiltonian $H_{l,0}(t)$ in order to identify the effective 2×2 YSR qubit Hamiltonian presented in the main text. That is achieved by another time-dependent unitary transformation

$$U_3(t) = \frac{1}{2\sqrt{BC}} \begin{bmatrix} -s_2 B_+ C_- e^{i\phi} & s_2 B_- C_+ e^{i\phi} & -s_2 B_+ C_+ e^{i\phi} & s_2 B_- C_- e^{i\phi} \\ s_1 B_- C_+ & -s_1 B_+ C_- & -s_1 B_- C_- & s_1 B_+ C_+ \\ s_1 s_2 C_+ B_+ & s_1 s_2 C_- B_- & -s_1 s_2 C_- B_+ & -s_1 s_2 B_- C_+ \\ B_- C_- & B_+ C_+ & B_- C_+ & C_- B_+ \end{bmatrix} \quad (\text{B1})$$

where

$$\begin{aligned}
t_h &= \frac{4\alpha_1\alpha_2}{\sqrt{2\pi k_F R}} e^{-R}, \\
B &= \sqrt{(2\alpha_2\alpha_1 - \alpha_1 - \alpha_2)^2 + (t_h \cos(k_F R + \pi/4) \sin(\theta/2))^2}, \\
C &= \sqrt{(\alpha_1 - \alpha_2)^2 + (t_h \sin(k_F R + \pi/4) \cos(\theta/2))^2}, \\
B_{\pm} &= \sqrt{B \pm (2\alpha_1\alpha_2 - \alpha_2 - \alpha_1)}, \\
C_{\pm} &= \sqrt{C \pm (\alpha_1 - \alpha_2)},
\end{aligned} \tag{B2}$$

with $s_1 = \text{sign}[\sin(k_F R + \pi/4)]$ and $s_2 = \text{sign}[\cos(k_F R + \pi/4)]$. Its effect on $H_l(t)$ can be formally written as:

$$\tilde{H}_l(t) = U_3^\dagger H_l(t) U_3 - i U_3^\dagger \dot{U}_3 = \tilde{H}_{l,0}(t) + \dot{\phi} \tilde{A}_{l,\phi}(t) + \dot{\theta} \tilde{A}_{l,\theta}(t), \tag{B3}$$

$$\tilde{H}_{l,0}(t) = U_3^\dagger H_{l,0}(t) U_3; \quad \tilde{A}_{l,s}(t) = U_3^\dagger A_{l,s} U_3 - i U_3^\dagger \partial_s U_3, \tag{B4}$$

with $s = \phi, \theta$. Note that while $\tilde{H}_{l,0}(t)$ is now diagonal, with energies $\pm E_{1,2}$, where $E_{1,2} = (B \pm C)/(2\alpha_1\alpha_2)$, the gauge field terms can induce transitions between its eigenstates. More importantly, these terms have two separate contributions: one from the initial gauge fields, originating from the first unitary transformations $U_{1,2}$, and one from the diagonalization of the 4×4 effective (instantaneous) time-dependent Hamiltonian $H_{l,0}(t)$. Both are required to correctly capture the low-energy sector dynamics, and starting from the static effective theory by turning the parameters θ and ϕ time-dependent would lead to erroneous results.

In order to establish a qubit that is well separated from the excited states, we assume that both $\alpha_1, \alpha_2 \neq 1$, as well as $t_h, \delta\alpha \ll 2\min|1 - \alpha_{1,2}|$, with $\delta\alpha = |\alpha_1 - \alpha_2|$. Then, we can further project $\tilde{H}_l(t)$ to the two lowest energy states, resulting in the qubit Hamiltonian presented in the main text (up to terms that act as identity in this subspace)

$$H_q(t) = \frac{\epsilon_q}{2} \Sigma_z + \beta(t) \cdot \Sigma, \tag{B5}$$

$$\begin{aligned}
\beta_z(t) &= \frac{\alpha_2 - \alpha_1}{2\alpha_1\alpha_2\epsilon_q} \sin^2(\theta/2) \dot{\phi}, \\
\beta_x(t) &= t_h \frac{\sin(k_F R + \pi/4) \sin\theta \sin(\theta/2)}{4\alpha_1\alpha_2\epsilon_q} \dot{\phi}, \\
\beta_y(t) &= t_h \frac{(\alpha_1 - \alpha_2) \sin(k_F R + \pi/4) \sin(\theta/2)}{4(\alpha_1\alpha_2)^2\epsilon_q^2} \dot{\theta},
\end{aligned} \tag{B6}$$

where $\epsilon_q = C/\alpha_1\alpha_2$ is the qubit splitting energy.

Appendix C: Details on the read out via torques

Here we provide details on the calculation of the torque $\boldsymbol{\tau} = -J_1 S \mathbf{n}_1 \times \langle \boldsymbol{\sigma}(0) \rangle$ acting on the precessing spin S_1 by the SC electrons, and its effects on the STM-ESR signal. We first note that at the operator level, the torque can be written as $\hat{\boldsymbol{\tau}} = -\mathbf{n}_1 \times \hat{\mathbf{h}}$, where we introduced the magnetic field operator $\hat{\mathbf{h}}(t) = \partial_{\mathbf{n}_1} H_{\text{tot}}(t)$. Then, for a given many-body state $|\Psi(t)\rangle$ that acts in the occupation number basis we have

$$\mathbf{h}_\Psi = \langle \Psi(t) | \hat{\mathbf{h}} | \Psi(t) \rangle = \langle \Psi(t) | \partial_{\mathbf{n}_1} H_{\text{tot}}(t) | \Psi(t) \rangle. \tag{C1}$$

For a static BdG Hamiltonian, we can write $H_{\text{tot}} = \sum_i \epsilon_i(\mathbf{n}_i) (\gamma_i^\dagger \gamma_i - 1/2)$, with $\epsilon_i(\mathbf{n}_i)$ being the BdG eigenvalues, and γ_i (γ_i^\dagger) being the Bogoliubov annihilation (creation) operator found from diagonalization. Then, in such a case we obtain the average field:

$$\mathbf{h} = \langle \hat{\mathbf{h}} \rangle = \sum_i (f_i - 1/2) \partial_{\mathbf{n}_1} \epsilon_i(\mathbf{n}_1), \tag{C2}$$

with $f_i = \langle \gamma_i^\dagger \gamma_i \rangle$ being the occupation of state i . This encodes both the well-known RKKY interaction mediated by the bulk states, as well as the (static) YSR contribution [90]. Dynamics can induce transitions between different instantaneous energy levels, and in general a full diagonal form for the BdG Hamiltonian might not be found. However,

in our perturbative scheme in the dynamics, when $\epsilon_q \neq 2\beta_z$, we can neglect the transitions caused by β_x and β_y . Moreover, since $\Omega_1 \ll \Delta$, the bulk states are also unaffected. Then, the many-body Hamiltonian is still diagonal, and the magnetic field reads:

$$\mathbf{h} = -\frac{1}{2} \sum_{i \in \text{bulk}} \partial_{\mathbf{n}_1} \epsilon_i(\mathbf{n}_1) + \sum_{i=1,2} (f_i - 1/2) \partial_{\mathbf{n}_1} \epsilon_i^{\text{eff}}(\mathbf{n}_1) \equiv \mathbf{h}_{\text{bulk}} + \mathbf{h}_{\text{YSR}}, \quad (\text{C3})$$

where the first and second terms determine the bulk contribution (all levels i empty, or $f_i = 0$) and YSR in-gap states contributions, respectively. Importantly, ϵ_i^{eff} are the full single-particle energies that include the shifts induced by the dynamics (which, in a more formal language, corresponds to Berry phase effects [65]). The YSR states that define the qubit states correspond in the many-body picture to the configurations $f_{1(2)} = 0(1)$ and $f_{1(2)} = 1(0)$. Thus, the field for each qubit state is

$$\mathbf{h}_\sigma = \mathbf{h}_{\text{bulk}} + \frac{(-1)^\sigma}{2} \partial_{\mathbf{n}_1} [\epsilon_1^{\text{eff}}(\mathbf{n}_1) - \epsilon_2^{\text{eff}}(\mathbf{n}_1)] \equiv \mathbf{h}_{\text{bulk}} + \frac{(-1)^\sigma}{2} (\mathbf{h}_s + \mathbf{h}_d), \quad (\text{C4})$$

with $\sigma = 0, 1$. Consequently, one can find the corresponding torques from $\boldsymbol{\tau}_\sigma = -\mathbf{n}_1 \times \mathbf{h}_\sigma$, $\boldsymbol{\tau}_s = -\mathbf{n}_1 \times \partial_{\mathbf{n}_1} \epsilon_q$ and $\boldsymbol{\tau}_d = -2\mathbf{n}_1 \times \partial_{\mathbf{n}_1} \beta_z$, as presented in the main text (note that these are more general as they assume arbitrary changes in the angles θ and ϕ).

For the numerical evaluation of the torques we have employed a Green function approach that describes the dimer when the target spin precesses circularly. In this case, an exact solution can be found, assuming $\phi(t) = \Omega t$ and $\theta = \text{const}$, with Ω being the precession frequency. Indeed, the dynamical problem in Eq. (A2) can be made static by rotating it with the time-dependent unitary transformation $\mathcal{U}(t) = e^{-i(\Omega/2)\sigma_z t}$. In this frame, the stationary Schrodinger equation from Eq. (A2) can be written as

$$\tilde{H}_{\text{BdG}} = H_{\text{BdG}}(0) - \frac{\Omega}{2} \sigma_z, \quad (\text{C5})$$

where the second term acts as a fictitious magnetic field on the superconductor. Following Ref. 60, the wave-function at any point \mathbf{r} can be written as, $\psi(\mathbf{r}) = \sum_{r_j \in 0, R} G_0(\mathbf{r} - \mathbf{r}_j, E) V_j \psi(\mathbf{r}_j)$, where

$$G_0(\mathbf{r}, E) = - \begin{bmatrix} (E + \Omega/2) I_0^+ + I_1^+ & 0 & I_0^+ & 0 \\ 0 & (E - \Omega/2) I_0^- + I_1^- & 0 & I_0^- \\ I_0^+ & 0 & (E + \Omega/2) I_0^+ - I_1^+ & 0 \\ 0 & I_0^- & 0 & (E - \Omega/2) I_0^- - I_1^- \end{bmatrix}, \quad (\text{C6})$$

with

$$I_0^\pm(r) = \int \frac{d\mathbf{k}}{(2\pi)^d} \frac{e^{i\mathbf{k}\cdot\mathbf{r}}}{1 + \epsilon_k^2 - (E \pm \Omega/2)^2}, \quad I_1^\pm(r) = \int \frac{d\mathbf{k}}{(2\pi)^d} \frac{\epsilon_k e^{i\mathbf{k}\cdot\mathbf{r}}}{1 + \epsilon_k^2 - (E \pm \Omega/2)^2}. \quad (\text{C7})$$

We then get the following set of eigenvalue equations:

$$\begin{aligned} (1 - G_0(0, E) V_1) \psi(0) &= G_0(R, E) V_2 \psi(R), \\ (1 - G_0(0, E) V_2) \psi(R) &= G_0(R, E) V_1 \psi(0), \end{aligned} \quad (\text{C8})$$

and the in-gap spectrum can be found numerically for arbitrary frequencies $\Omega/2 < 1$ from the 8×8 determinant

$$\begin{vmatrix} 1 - G_0(0, E) V_1 & G_0(R, E) V_2 \\ G_0(R, E) V_1 & 1 - G_0(0, E) V_2 \end{vmatrix} = 0. \quad (\text{C9})$$

Then, the associated torques (that include all orders in $\Omega/2$) can be evaluated as in the previous subsection. The plots depicted in Fig. 4 in the main text were obtained assuming the deep Shiba limit ($\alpha_{1,2} \sim 1$) and $\Omega/2 \ll 1$ (adiabatic driving), which is the relevant regime in this work. Nevertheless, this approach can be readily employed to study the effects of the dynamics beyond the adiabatic realm.

Appendix D: Linearization of LLG equation and resonance frequency renormalization

The LLG equation describing the dynamics of the classical spin \mathbf{S}_1 in the presence of the torque $\boldsymbol{\tau}_\sigma$ torque pertaining to the YSR qubit in state $\sigma = 0, 1$ can be written as

$$\dot{\mathbf{S}}_1(t) = -\gamma \mathbf{S}_1(t) \times \mathbf{B}(t) + \boldsymbol{\tau}_\sigma(t) + \alpha_g \mathbf{S}_1 \times \dot{\mathbf{S}}_1, \quad (\text{D1})$$

where $\mathbf{B}(t) = B_0\mathbf{z} + \mathbf{B}_\perp(t)$ is the external magnetic field, being the sum of a constant term along z which defines the bare resonance frequency $\Omega_0 = \gamma B_0$, and a weak in-plane rf component. Specifically, we consider $\mathbf{B}_\perp(t) = B_\perp(\cos(\Omega_1 t), \sin(\Omega_1 t), 0)$ and $B_\perp \ll B_0$. In the stationary limit, the impurity spin can be written as $\mathbf{S}_1(t) = S_z\mathbf{z} + \delta\mathbf{S}(t)$, with $\delta\mathbf{S}(t) = S_\perp(\cos(\Omega_1 t + \phi), \sin(\Omega_1 t + \phi), 0)$, where $S_\perp = S \sin \theta \approx S\theta$ and $S_z = S \cos \theta \approx S$, and ϕ quantifies the lagging of the spin with respect to the driving field. In this limit, we can also expand the torque $\boldsymbol{\tau}_\sigma$ in terms of the small parameter θ , which in turn gives [65]:

$$\left[\alpha_g \Omega_1 S + \left(\Omega_1 - \Omega_0 + \frac{\tau'_{\sigma s}}{S} + \Omega_1 \frac{\tau'_{\sigma d}}{S} \right) \mathbf{z} \times \right] \delta\mathbf{S}(t) \approx -\gamma S \mathbf{z} \times \mathbf{B}_\perp(t), \quad (\text{D2})$$

where $\tau'_{\sigma s} = (\partial\tau_{\sigma s}/\partial\theta)|_{\theta=0}$ and $\tau'_{\sigma d} = (\partial\tau_{\sigma d}/\partial\theta)|_{\theta=0}$ with $\tau_{\sigma b} = (\partial\tau_{\sigma d}/\partial\Omega_1)|_{\Omega_1=0}$.

From the above equations, we can readily evaluate both the amplitude S_\perp and the phase lag ϕ , respectively:

$$S_\perp = \frac{\gamma S B_\perp}{\sqrt{(\Omega_1 - \Omega_0 + \tau'_{\sigma s}/S + \tau'_{\sigma d}\Omega_1/S)^2 + (\alpha_g S \Omega_1)^2}}, \quad (\text{D3})$$

$$\phi = \arctan \frac{\alpha_g S \Omega_1}{\Omega_1 - \Omega_0 + \tau'_{\sigma s}/S + \tau'_{\sigma d}\Omega_1/S}. \quad (\text{D4})$$

The resonance frequency $\Omega_{r,\sigma}$ of the precessing spin is shifted depending on the qubit state $\sigma = 0, 1$ as

$$\Omega_{r,\sigma} = \frac{\Omega_0 - \frac{\tau'_{\sigma s}}{S}}{1 + \frac{\tau'_{\sigma d}}{S}} \approx \Omega_0 \left(1 - \frac{\tau'_{\sigma d}}{S} \right) - \frac{\tau'_{\sigma s}}{S}. \quad (\text{D5})$$

Note that each type of torque will also contain a constant contribution, independent of the qubit state, that originates from the (occupied) bulk states. Hence, we can write $\tau'_{\sigma s} \rightarrow \tau'_{bs} + \tau'_{\sigma s}$ and $\tau'_{\sigma d} \rightarrow \tau'_{bd} + \tau'_{\sigma d}$, where the index b labels bulk contribution. Nevertheless, as showed in Ref. [90] the static bulk contribution is negligible for $R \geq 1$, while as argued in Ref. [65], the dynamical contribution of the bulk states is negligible in the adiabatic regime. We can then extract the resonance frequency difference as

$$\delta\Omega = \Omega_{r,0} - \Omega_{r,1} \approx \frac{1}{S} (\Omega_0 \tau'_d + \tau'_s), \quad (\text{D6})$$

which reflects only the in-gap state effects.

Appendix E: Manipulation of the YSR qubit: Rabi oscillations

a. Behavior of Rabi oscillation period around $\theta = 0$ and π

The Rabi frequency and hence, the time period of the Rabi oscillation is determined by β_x . Notably, the β_i terms are much weaker for deviation $\delta\theta$ around $\theta = 0$ as compared to such deviation around $\theta = \pi$ making it inefficient for manipulation in the parallel configuration. In Fig. 6a we show β_x as a function of $\delta\theta$ near $\theta = 0$ and near π , suggesting that β_x varies linearly (quadratically) around $\theta = \pi$ ($\theta = 0$).

1. Numerical approach for qubit state evolution

The time evolution operator corresponding to the qubit Hamiltonian can be written as $U(t, t_0) = \mathcal{T} e^{-\frac{i}{\hbar} \int_{t_0}^t dt' H_q(t')}$, where \mathcal{T} represents the time ordering operator. We have implemented the evolution of the qubit state by performing time slicing with small increment δt , so that the evolution operator during one slice can be expanded as $U(t, t - \delta t) = 1 - (i/\hbar)H_q(t)\delta t$. Then, starting from the initial state $|0\rangle$, the qubit state at time t can then be written as

$$|\psi(t)\rangle = U(t, 0)|0\rangle = U(t, t - \delta t)U(t - \delta t, t - 2\delta t) \cdots U(\delta t, 0)|0\rangle, \quad (\text{E1})$$

which we evaluate numerically for $|\psi(t)\rangle$ by evolving the state under the sequence of pulses described in the main text.

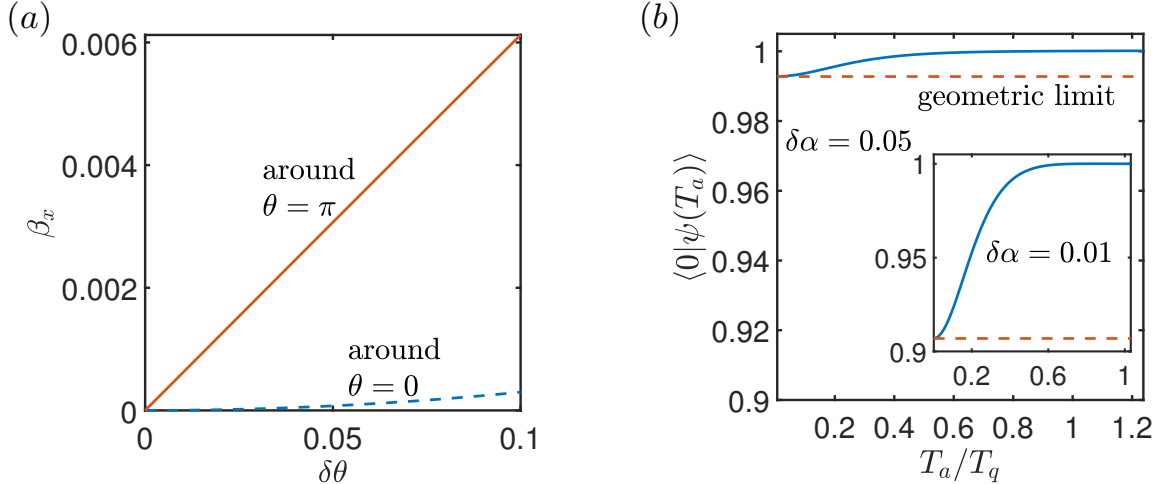


FIG. 6. (a) The Rabi oscillation strength β_x in Eq. (7) as a function of the deviation $\delta\theta$ around $\theta = 0$ (blue dashed line) and π (red solid line) for $\alpha_1 = 1.15$, $\alpha_2 = 1.1$, and $R = 2.9$. Note that for these parameters, $t_h/\delta\alpha = 0.34$. (b) The probability amplitude of the qubit initialized in state $|0\rangle$ to remain in that state after time T_a , $\langle 0 | \psi(T_a) \rangle$, in terms of $T_q = \hbar/\epsilon_q$ for $\delta\alpha = 0.05$, or $t_h/\delta\alpha = 0.34$ (inset $\delta\alpha = 0.01$, or $t_h/\delta\alpha = 1.75$). The blue curve is the result obtained from the full numerical implementation of the evolution, while the red-dashed line is $\langle 0 | \psi(T_a) \rangle$ evaluated in the geometrical limit using Eq. (E2). As T_a is increased, the full curve starts deviating from the geometric limit valid for $T_a \ll T_q$, and reaches almost unity already for $T_a \sim T_q$, consistent with the adiabatic result. All plots are obtained using $k_F = 13.55$.

2. Analytical approach for qubit state evolution in the geometric regime

The qubit state evolution subjected to the pulse $\theta(t) = \pi \tanh(2\pi t/T_a)$ can be studied analytically in two extreme limits: the adiabatic ($T_a \gg T_q$) and geometric ($T_a \ll T_q$) limit, respectively. In the adiabatic limit, the qubit evolution is trivial, as it remains in state $|0\rangle$ during the pulse. In the geometric limit, the energy splitting ϵ_q becomes unimportant (thus can be neglected), and the qubit evolution is solely determined by $\beta_y \Sigma_y \propto \dot{\theta}$. Then, the evolution operator under an arbitrary rotation of the qubit from $\theta = 0$ to a final θ_0 reads $U_g(\theta_0) = e^{-i \int \beta_y \Sigma_y dt} \equiv \cos A(\theta_0) - i \sin A(\theta_0) \Sigma_y$, where

$$\begin{aligned} A(\theta_0) &= \int_0^{\theta_0} d\theta \frac{\delta\alpha t_h \sin(k_F R + \pi/4) \sin(\theta/2)}{4(\delta\alpha^2 + (t_h \sin(k_F R + \pi/4) \cos(\theta/2))^2)} \\ &= \frac{1}{2} \left[\tan^{-1} \left(\frac{t_h \sin(k_F R + \pi/4)}{\delta\alpha} \right) - \tan^{-1} \left(\frac{t_h \sin(k_F R + \pi/4) \cos(\theta_0/2)}{\delta\alpha} \right) \right], \end{aligned} \quad (\text{E2})$$

and thus the first pulse in Fig. 3a corresponds to $\theta_0 = \pi$ in the geometric limits.

Fig. 6b shows the probability amplitude of the qubit state to be in $|0\rangle$ as a function of time T_a (scaled with T_q), $c_0(T_a)$, starting from $|0\rangle$. The blue solid line represents c_0 evaluated numerically while the red dashed line corresponds to the geometric limit evaluated as $c_0 = \cos A(\pi)$. The deviation of the geometric amplitude from adiabatic result increases with decreasing $\delta\alpha$, which is due to the effect of tunneling that makes it easier for the qubit to explore the Bloch sphere. For $\delta\alpha > \epsilon_q$, the deviation is negligible and $c_0(T_a)$ depends weakly on the pulse length T_a . Thus, this situation is preferable for the qubit manipulation.

3. Geometric effects around $\theta = \pi$

The Rabi oscillations amplitude is also reduced because the geometric pulse $\theta(t) = (\pi - \delta\theta) \tanh(2\pi t/T_b)$ leads to a probability amplitude c_1 to excite the qubit from state $|0\rangle$ to state $|1\rangle$. Assuming that $t_h < \delta\alpha$ and $\delta\theta \ll 1$, we obtain

$$c_1 \approx \frac{t_h \sin(k_F R + \pi/4)}{4\delta\alpha} \delta\theta. \quad (\text{E3})$$

This linear increase of c_1 with $\delta\theta$ shows good agreement with the full numerical results, as shown in Fig. 7 for various values of $\delta\alpha$. In the limit $t_h \ll \delta\alpha$, $c_1 \rightarrow 0$ and the amplitude of Rabi oscillations approaches unity, as argued in the main text.

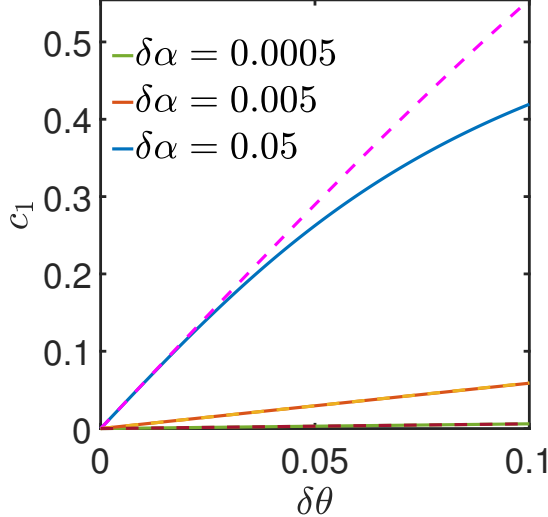


FIG. 7. The dependence of c_1 on $\delta\theta$ near $\theta = \pi$ for $\delta\alpha = 0.0005, 0.005, 0.05$, and which corresponds to $t_h/\delta\alpha = 34, 3.4, 0.34$ at $R = 2.9$. We see that for $\delta\alpha$ such that $t_h/\delta\alpha \leq 1$, the weight c_1 increases linearly with $\delta\theta$, matching well the geometric limit in Eq. (E3), represented by the dashed lines, for a wide range of deviations $\delta\theta$.

Appendix F: Decoherence of YSR qubit

Below we give the detailed analysis of the decoherence in the YSR qubit induced due to the fluctuations in the magnetic moments and phonon coupling to the Shiba electrons.

1. Magnon-induced decoherence

Here we provide details on the decoherence of the YSR qubit by the stochastic fluctuations in the magnetic moments orientations. The fluctuations of the spin $k = 1, 2$ can be accounted for by performing the substitution $\mathbf{n}_k \rightarrow \mathbf{n}_k + \delta\mathbf{n}_k(t)$, where $\delta\mathbf{n}_k(t) = \mathbf{e}_{k,1}\delta n_{k,1} + \mathbf{e}_{k,2}\delta n_{k,2} \perp \mathbf{n}_k$ describe the induced fluctuations of the magnetic moment perpendicular to the deterministic orientations \mathbf{n}_k . Here, $\mathbf{e}_{k,i}$ and $\delta n_{k,i}$ with $i = 1, 2$ label the orthogonal fluctuations directions and the corresponding magnitudes, respectively, with $\mathbf{e}_{k,1} = \frac{\mathbf{z} \times \mathbf{n}_k}{|\mathbf{z} \times \mathbf{n}_k|}$ and $\mathbf{e}_{k,2} = \frac{\mathbf{n}_k \times (\mathbf{z} \times \mathbf{n}_k)}{|\mathbf{n}_k \times (\mathbf{z} \times \mathbf{n}_k)|}$.

Then, the coupling between the qubit and the classical spins changes accordingly, $V \rightarrow V + \delta V(t)$, with

$$\delta V(t) = \sum_{k=1,2} J_k S \delta\mathbf{n}_k(t) \cdot \boldsymbol{\sigma} \delta(\mathbf{r} - \mathbf{r}_k) = \sum_{k=1,2} \frac{\partial H_{\text{BdG}}}{\partial \mathbf{n}_k} \cdot \delta\mathbf{n}_k(t) \equiv \sum_{k=1,2} \hat{\mathbf{h}}_k \cdot \delta\mathbf{n}_k(t), \quad (\text{F1})$$

where $\hat{\mathbf{h}}_k$ is the magnetic field operator acting on the electrons.

Projecting the above Hamiltonian onto the qubit subspace, leads to the following extra contribution:

$$\delta H_q(t) = \sum_k \sum_{\mu=1,2; \nu=x,y,z} \delta n_{k,\mu}(t) \chi_k^{\mu\nu} \Sigma_\nu, \quad (\text{F2})$$

where $\chi_k^{\mu\nu}$ represent the components of the tensor coupling between the fluctuations and the qubit, and which can be extracted from above:

$$\chi_k^{\mu\nu} = \frac{1}{2} \text{Tr}[\mathbf{e}_{k,\mu} \cdot \hat{\mathbf{h}}_k \Sigma_\nu], \quad (\text{F3})$$

with the trace being taken over the qubit states. In the following, we assume the external driving is absent, and only focus on the static coherence properties. Then, we can evaluate explicitly the matrix elements of the field:

$$\langle \sigma | \hat{\mathbf{h}}_k | \sigma \rangle = -(-1)^\sigma \frac{1}{2} \partial_{\mathbf{n}_k} \epsilon_q = (-1)^{\sigma+k} \frac{1}{2} \partial_\theta \epsilon_q \mathbf{e}_{k,2}, \quad (\text{F4})$$

$$\langle \sigma | \hat{\mathbf{h}}_k | \bar{\sigma} \rangle = (-1)^\sigma \epsilon_q \langle \sigma | \partial_{\mathbf{n}_k} \bar{\sigma} \rangle = -(-1)^{\sigma+k} \epsilon_q \left[\langle \sigma | \partial_\theta \bar{\sigma} \rangle \mathbf{e}_{k,2} + \frac{1}{\sin \theta} \langle \sigma | \partial_\phi \bar{\sigma} \rangle \mathbf{e}_{k,1} \right], \quad (\text{F5})$$

where the factor $(-1)^k$ reflects that the magnetic fields are opposite for given relative angles. Note that for $\delta\alpha \neq 0$, the diagonal terms vanish at both $\theta = 0$ and $\theta = \pi$. From the above expressions, we can write the total magnetic field operator acting in the qubit subspace as:

$$\hat{\mathbf{h}}_k^q = (-1)^k \left[\frac{1}{2} \partial_\theta \epsilon_q \Sigma_z \mathbf{e}_{k,2} - \epsilon_q \left(\beta'_y \Sigma_x \mathbf{e}_{k,2} + \frac{\beta'_x}{\sin \theta} \Sigma_y \mathbf{e}_{k,1} \right) \right], \quad (\text{F6})$$

where $\beta'_x = \beta_x/\dot{\phi}$ and $\beta'_y = \beta_y/\dot{\theta}$ in the qubit Hamiltonian in Eq. (B6). From here, the matrix $\chi_k^{\mu\nu}$ can be readily identified. Let us evaluate the above field for the two cases of interest $\theta = 0$ (parallel) and $\theta = \pi$ (anti-parallel) configurations, respectively. In the former case, $\hat{\mathbf{h}}_k^q \equiv 0$, meaning that no dephasing or relaxation occurs because of the coupling to the magnetic fluctuations, while in the latter $\hat{\mathbf{h}}_k^q = (-1)^{k+1} g_c (\Sigma_x \mathbf{e}_{k,2} + \Sigma_y \mathbf{e}_{k,1})$ where

$$g_c = \frac{t_h \sin(k_F R + \pi/4)}{4\alpha_1 \alpha_2}, \quad (\text{F7})$$

is the effective coupling strength of the qubit to the fluctuations whose magnitude is dictated by the tunneling t_h . For this specific orientation, Eq. (F2) becomes:

$$\delta H_q(t) = g_c \sum_k (-1)^{k+1} [\delta n_{k,2}(t) \Sigma_x + \delta n_{k,1}(t) \Sigma_y]. \quad (\text{F8})$$

We are now in position to calculate the decoherence rates engendered by this coupling. We first introduce the noise power spectrum pertaining to the fluctuations $\delta \mathbf{n}_k(t)$ in the Fourier space:

$$S_{\mu\nu}^{kk'}(\omega) = \frac{1}{2\pi} \int dt e^{-i\omega t} \langle \delta n_{k,\mu}(t) \delta n_{k',\nu}(0) \rangle \delta_{kk'} \equiv S_{\mu\nu}^k(\omega), \quad (\text{F9})$$

where the averages are taken over the thermal equilibrium, and we assumed the fluctuations of the two spins are not correlated. Within the Bloch-Redfield framework [3], the dephasing and the longitudinal relaxation rates read, respectively:

$$\Gamma_{\phi,m} = \sum_{k=1,2} (|\chi_k^{1z}|^2 + |\chi_k^{2z}|^2) S_{11}^k(0), \quad (\text{F10})$$

$$\Gamma_{1,m} = \sum_{\mu,\nu} \sum_{k=1,2; \sigma=\pm} \chi_k^{\mu\sigma} \chi_k^{\nu\bar{\sigma}} S_{\mu\nu}^k(\sigma \epsilon_q), \quad (\text{F11})$$

where $\chi_k^{\mu\pm} = \chi_k^{\mu x} \pm i \chi_k^{\mu y}$. The pure dephasing rate Γ_ϕ vanishes at both $\theta = 0$ and π , and $\Gamma_{1,m} = 0$ at $\theta = 0$. The relaxation rate at $\theta = \pi$ is

$$\Gamma_{1,m} = 1/T_{1,m} = 2g_c^2 \sum_{k=1,2} [S_{11}^k(\epsilon_q) + S_{11}^k(-\epsilon_q) - i(S_{12}^k(-\epsilon_q) - S_{12}^k(\epsilon_q))], \quad (\text{F12})$$

while the dephasing time satisfies $T_{2,m} = 2T_{1,m}$. In order to give estimates, we need to describe the noise spectrum of the magnetic fluctuations. To do that, we start by employing the stochastic LLG equation describing the magnets in the presence of magnetic noises (here we disregard the effect of the qubit on the dynamics, as it would only manifest in higher orders in the coupling):

$$\dot{\mathbf{n}}_k = -\gamma \mathbf{n}_k \times \left(\mathbf{B}_{k,\text{eff}} + \delta \mathbf{B}_k(t) \right) + \alpha_g \mathbf{n}_k \times \dot{\mathbf{n}}_k. \quad (\text{F13})$$

Here $\mathbf{B}_{k,\text{eff}} = -\gamma^{-1} \delta F_S(\mathbf{n}_k)/\delta \mathbf{n}_k$ is the effective magnetic field acting on the impurity with $F_S(\mathbf{n}_k)$ being the k^{th} classical spin free energy, and $\delta \mathbf{B}_k(t)$ is the stochastic magnetic field whose Fourier components $\delta B_{k,\mu}(\omega)$ with $\mu = \mathbf{e}_{k,1}, \mathbf{e}_{k,2}$ satisfy the fluctuation-dissipation relation [86]:

$$\langle \delta B_{k,\mu}(\omega) \delta B_{k',\nu}(\omega') \rangle = \underbrace{\frac{\alpha_g \hbar \omega}{\gamma^2 S} \left(\coth \left(\frac{\hbar \omega}{2k_B T} \right) - 1 \right)}_{S(\omega, T)} \delta(\omega + \omega') \delta_{\mu\nu} \delta_{k,k'}. \quad (\text{F14})$$

In order to describe the experimental observations [87, 89], we assume z to be an easy-axis (the spin orients perpendicular to the surface), so that the free energy can be written as in the main text:

$$F_S(\mathbf{n}_k) = -\frac{\kappa}{2}n_{k,z}^2 - \gamma\mathbf{B}\cdot\mathbf{n}_k, \quad (\text{F15})$$

where $\mathbf{B} = B_z\mathbf{z}$ is external magnetic field along z and κ is the strength of the anisotropy, which is assumed to be identical for the two spins. Consequently, the effective magnetic field that determines the dynamics can then be written as $\mathbf{B}_{k,\text{eff}} = B_{k,\text{eff}}\mathbf{z}$, with the magnitude $B_{k,\text{eff}} = B_z + (\kappa/\gamma)n_{k,z}$. For the anti-parallel alignment and considering the deterministic direction of the spins to be along the z -axis, inserting the effective field in the LLG equation, we can extract the noise spectrum, for which we find

$$\begin{aligned} S_{11}^k &= S_{22}^k = \gamma^2 \frac{(\gamma B_{k,\text{eff}})^2 + (\alpha_g\omega)^2 + \omega^2}{[(\gamma B_{k,\text{eff}} - \omega)^2 + (\alpha_g\omega)^2][(\gamma B_{k,\text{eff}} + \omega)^2 + (\alpha_g\omega)^2]} S(\omega, T), \\ S_{12}^k &= -S_{21}^k = -2i\gamma^2 \frac{(-1)^k \omega \gamma B_{k,\text{eff}}}{[(\gamma B_{k,\text{eff}} - \omega)^2 + (\alpha_g\omega)^2][(\gamma B_{k,\text{eff}} + \omega)^2 + (\alpha_g\omega)^2]} S(\omega, T), \end{aligned} \quad (\text{F16})$$

where $k = 1, 2$. To give some estimates, we assume $\alpha_1 = 1.15$, $\alpha_2 = 1.1$, $R = 2.9$, $\alpha_g = 0.001$. Considering magnetization anisotropy energy $\kappa = 0.1$ meV and $\Omega_0 = 25$ GHz, we find $T_{2,m} \approx 7\mu\text{s}$ allowing around 800 Rabi oscillations to be experimentally observable before the qubit is hampered by the decoherence stemming from magnetic fluctuations. In the presence of a small applied magnetic field, say, $B_z = 0.2$ T which corresponds to $\Omega_0 = 30.5$ GHz, $T_{2,m} \approx 4.5\mu\text{s}$ allowing around 500 Rabi oscillations to be experimentally observable.

2. Decoherence induced by the electron-phonon coupling

The electron-phonon coupling Hamiltonian can be written as [1]

$$H_{e-ph} = \frac{1}{2}g_{ph} \int d\mathbf{r} \Psi^\dagger(\mathbf{r}) \tau_z \Psi(\mathbf{r}) \Phi(\mathbf{r}), \quad (\text{F17})$$

$$\Phi(\mathbf{r}) = \sum_{\mathbf{q}} \sqrt{\frac{\hbar\omega_{\mathbf{q}}}{2V_0}} (b_{\mathbf{q}} e^{i\mathbf{q}\cdot\mathbf{r}} + b_{\mathbf{q}}^\dagger e^{-i\mathbf{q}\cdot\mathbf{r}}), \quad (\text{F18})$$

where $\Psi(\mathbf{r}) = (\psi_\uparrow^\dagger(\mathbf{r}), \psi_\downarrow^\dagger(\mathbf{r}), \psi_\downarrow(\mathbf{r}), -\psi_\uparrow(\mathbf{r}))^T$ is the electron field operator written in the spin and Nambu basis, $b_{\mathbf{q}}$ ($b_{\mathbf{q}}^\dagger$) is the phonon annihilation (creation) operator with momentum \mathbf{q} , speed velocity c_s , and frequency $\omega_{\mathbf{q}} = c_s q$ (assuming only acoustic phonons) in the SC of volume V_0 . This interaction is quantified by the coupling strength $g_{ph} = \frac{Z\hbar^2\pi^2 n_0}{mk_F\sqrt{B}}$, where Z , n_0 , B are the electron valence from the SC, atomic density and adiabatic bulk modulus, respectively [2]. The electronic field operator describing the low-energy YSR states can be written as [61]:

$$\Psi(\mathbf{r}) \approx \sum_{i=1,2} \phi_{i+}(\mathbf{r}) \gamma_i + \phi_{i-}(\mathbf{r}) \gamma_i^\dagger, \quad (\text{F19})$$

where γ_i (γ_i^\dagger) are the annihilation (creation) operators for the in-gap Shiba state at position $i = 1, 2$, while

$$\phi_{i+}(\mathbf{r}) = \frac{JS}{\sqrt{N_i}} U_i \begin{bmatrix} (E_{i+} + \Delta) I_0(\mathbf{r}) + I_1(\mathbf{r}) \\ 0 \\ (E_{i+} + \Delta) I_0(\mathbf{r}) - I_1(\mathbf{r}) \\ 0 \end{bmatrix}, \quad (\text{F20})$$

and $\phi_{i-}(\mathbf{r}) = \tau_y \sigma_y K \phi_{i+}(\mathbf{r})$ are the eigen-spinors pertaining to energies $E_{i\pm} = \pm\Delta(1 - \alpha_i^2)/(1 + \alpha_i^2)$, with K being the complex conjugation. Here, $U_i \equiv U(S_i)$ are unitary matrices that align the quantization axis of the Nambu spinor with the direction of impurity spin $i = 1, 2$, and $N_i = \frac{(1+\alpha_i^2)^2}{2\pi\nu\Delta\alpha_i}$ is the normalization constant for the i th YSR state. The electron-phonon coupling Hamiltonian acting in the low-energy space spanned by the two YSR states can then be written as

$$H_{e-ph} = \frac{g_{ph}}{2} \sum_{\mathbf{q}} \sqrt{\frac{\hbar\omega_{\mathbf{q}}}{2V_0}} (b_{\mathbf{q}} + b_{-\mathbf{q}}^\dagger) [I_{ij}^o(\mathbf{q}) \gamma_i^\dagger \gamma_j + I_{ij}^e(\mathbf{q}) \gamma_i^\dagger \gamma_j^\dagger + \text{h.c.}], \quad (\text{F21})$$

$$I_{ij}^{o,e}(\mathbf{q}) = \int d\mathbf{r} e^{i\mathbf{q}\cdot\mathbf{r}} [\phi_{1+}^\dagger(\mathbf{r}) \tau_z \phi_{2\pm}(\mathbf{r}) - \phi_{2\mp}^\dagger(\mathbf{r}) \tau_z \phi_{1-}(\mathbf{r})], \quad (\text{F22})$$

being overlap integrals between the YSR states and the phonon field. In the limit $\mathbf{q} \cdot \mathbf{R} \ll 1$, we can approximate $I_{ij}^{o,e}(\mathbf{q})$ with its $\mathbf{q} = 0$ expression. We have checked numerically that this condition is met in our setup, consequence of the interplay between the phonon energy $\omega_q = c_s q$ which needs to match the qubit splitting, and the inter-impurity distance R . Furthermore, the YSR qubit acts in the odd-parity subspace, and thus only the $I_{ij}^o(0)$ integrals will be discussed in the following. Considering $k_F R \gg 1$,

$$I_{12}^o(0) \approx \frac{2t_h \cos(k_F R + \pi/4)(\alpha_1 + \alpha_2)}{(1 + \alpha_1^2)(1 + \alpha_2^2)\sqrt{\alpha_1 \alpha_2}} \frac{R}{\xi} \cos \frac{\theta}{2}, \quad (\text{F23})$$

while we obtain $I_{jj}^{o,e}(0) = 0$, which is in itself a novel result (this holds when linearisation of the spectrum around the Fermi level is performed). To evaluate the relaxation, we need to write the above Hamiltonian in the qubit basis. We obtain:

$$H_{q-ph} = \frac{g_{ph}}{2\alpha_1 \alpha_2 \epsilon_q} I_{12}^o(0) \sum_{\mathbf{q}} \sqrt{\frac{\hbar \omega_{\mathbf{q}}}{2V_0}} (b_{\mathbf{q}} + b_{-\mathbf{q}}^\dagger) \left(\delta\alpha \Sigma_x + t_h \sin(k_F R + \pi/4) \cos \frac{\theta}{2} \Sigma_z \right), \quad (\text{F24})$$

which vanishes in the limit $t_h \rightarrow 0$, as expected. Moreover, it entails to both population relaxation ($T_{1,ph}$), as well as pure dephasing ($T_{\phi,ph}$).

The phonon-induced relaxation time $T_{1,ph}$ can be found analogously to $T_{1,m}$ pertaining to the impurities fluctuations calculation. Then, from Eq. (F23) the relaxation rate can be evaluated as

$$\Gamma_{1,ph} = \frac{2\pi g_{ph}^2 (\delta\alpha)^2}{4\hbar e_q^2 \alpha_1^2 \alpha_2^2} |I_{12}^o(0)|^2 \int \frac{d\mathbf{q}}{4\pi^2 x} \hbar \omega_q (2n_q + 1) \delta(\epsilon_q - \hbar \omega_{\mathbf{q}}) = \left(\frac{g_{ph} |I_{12}^o(0)| \delta\alpha}{2\hbar c_s \alpha_1 \alpha_2} \right)^2 \frac{1}{\hbar x} (2n(\epsilon_q) + 1), \quad (\text{F25})$$

where x is the thickness of the 2D SC. We can readily see that $\Gamma_{1,ph} \propto \cos^2(\theta/2)$, vanishing in the anti-parallel configuration, while becoming maximal in the parallel one. This is in stark contrast to the relaxation induced by impurities fluctuations, $\Gamma_{1,m} \propto \sin^2(\theta/2)$, which vanishes in the parallel configuration. Consequently, the two mechanisms do not compete with each other in the two qubit operation configurations, allowing to separately extract their effects. The reason for such behaviour is that phonons cannot cause spin-flip transitions during the tunneling processes. In the anti-parallel configuration, the tunneling of the YSR quasi-particles involve spin-flips, and thus results in zero coupling. The pure dephasing rate $\Gamma_{\phi,ph} = 0$, consequence of the phonon power spectrum $J_{ph}(\omega) \propto \omega^2$ in the current 2D setup [3]. Then, similarly to magnons, the phonon-induced dephasing entirely originates from longitudinal relaxation, or $T_{2,ph} = 2T_{1,ph}$.

In order to give estimates, let us focus on a 2D Pb SC slab. We assume $x = 10$ nm, i.e. much smaller than the coherence length ξ , $c_s \approx 10^4$ m/s, and $g_{ph} \approx 1.2 \times 10^{-8} \sqrt{\mu\text{eVcm}^3}$. This leads to $\Gamma_{1,ph}(\theta) = 1.72 \times 10^5 \cos^2(\theta/2) \text{ s}^{-1}$, reaching its maximum at $\theta = 0$. The corresponding phonon-induced relaxation time in the parallel configuration is then $T_{1,ph} \approx 5.8 \mu\text{s}$, comparable in magnitude to that stemming from impurity fluctuations.

Appendix G: Electron-photon coupling in a cavity QED setup

Next we evaluate the effect of photons (e.g. originating from a microwave cavity coupled to the YSRQ for manipulation and measurement purposes). The electron-photon coupling Hamiltonian reads [61]

$$H_{e-phot} = \frac{1}{2} \int d\mathbf{r} \Psi^\dagger(\mathbf{r}) [\mathbf{A}(t) \cdot \hat{\mathbf{J}} + \hat{\mathbf{J}} \cdot \mathbf{A}(t)] \Psi(\mathbf{r}) \approx \sum_{i,j=1,2} M_{ij}^o(t) \gamma_i^\dagger \gamma_j + M_{ij}^e(t) \gamma_i^\dagger \gamma_j^\dagger + h.c.,$$

$$M_{ij}^{e,o}(t) = \int d\mathbf{r} \mathbf{A}(t) \cdot \mathbf{J}(\mathbf{r}), \quad (\text{G1})$$

$$\mathbf{J}_{ij}^{e,o}(\mathbf{r}) = \frac{e\hbar}{2mi} [\phi_{i\pm}^\dagger(\mathbf{r}) \nabla \phi_{j+}(\mathbf{r}) - \phi_{j\mp}^\dagger(\mathbf{r}) \nabla \phi_{i-}(\mathbf{r})], \quad (\text{G2})$$

where the $\hat{\mathbf{J}}$ is the current operator that couples to the vector potential $\mathbf{A}(t)$ of the electromagnetic field via the substitution $-i\hbar\nabla \rightarrow -i\hbar\nabla + e\mathbf{A}(t)$. For simplicity, we assume $\mathbf{A}(t)$ constant in space over the size of the YSRQ, since the wavelength of the photons resonant with ϵ_q are longer than the coherence length. We mention that the diagonal terms $M_{jj}^o(t) = 0$, since the localized states do not carry any current. Using $\mathcal{E}(t) = -\partial\mathbf{A}(t)/\partial t$, with $\mathcal{E}(t)$ being the electric field, allows to write for the odd-parity sector term in the Fourier space:

$$|M_{12}^o(\omega)| \approx \frac{e\Delta\xi \mathcal{E}(\omega) \cdot \hat{\mathbf{R}}}{\hbar\omega} \frac{t_h \cos(\theta/2) \cos(k_F R + \pi/4)}{\sqrt{\alpha_1 \alpha_2} (1 + \alpha_1^2)(1 + \alpha_2^2)} \left[1 + \alpha_1 \alpha_2 + \frac{R}{\xi} (\alpha_1 \alpha_2 - 1) \right], \quad (\text{G3})$$

where we utilised $i\omega \mathbf{A}(\omega) = \mathcal{E}(\omega)$ and $\hat{\mathbf{R}} = \mathbf{R}/R$. To give estimates for the coupling strength, we note that in microwave cavities with frequencies comparable to the qubit splitting the electric field can be as large as $\mathcal{E} \approx 0.2$ V/m [4] which, when using the same YSRQ parameters as in the previous section, leads to a coupling strength $|M_{12}^o(\epsilon_q)|/\hbar \approx 10$ MHz in the parallel alignment of the magnetic impurities.

-
- [1] D. Olivares, A. L. Yeyati, L. Bretheau, Ç. Girit, H. Pothier, and C. Urbina, Physical Review B **89**, 104504 (2014).
 - [2] A. L. Fetter and J. D. Walecka, Quantum theory of many-particle systems (Courier Corporation, 2012).
 - [3] K. Blum, Density matrix theory and applications, vol. 64 (Springer Science & Business Media, 2012).
 - [4] A. Blais, A. L. Grimsmo, S. Girvin, and A. Wallraff, Reviews of Modern Physics **93**, 025005 (2021).